Miguel Martim Chambel Simão



Bachelor's degree in Micro and Nanotechnology Engineering

Skin sensors for health care: paper-based flexible and wearable pressure sensor

Dissertation for the obtainment of the degree of Master in Micro and Nanotechnology Engineering

Supervisors:

Dr. Elvira Fortunato, Full Professor, FCT-UNL

Dr. Ana Pimentel, Pos-Doc Researcher, FCT-UNL

Jury

President: Prof. Dr. Rodrigo Ferrão de Paiva Martins

Arguent: Prof. Dr. Joana Maria Dória Vaz Pinto Morais Sarmento

Vowel: Dr. Ana Cláudia Madeira Botas Gomes Pimentel

September, 2021



| Skin sensors for health care: paper-based flexible and wearable pressure sensor |
|-------------------------------------------------------------------------------------------------------------------------------------------------------------------------------------------------------------------------------------------------------------------------------------------------------------------------------------------------------------------------------------------------------------------------------------------------------------------------------------------------------------------------|
| Copyright © Miguel Martim Chambel Simão, Faculdade de Ciências e Tecnologia, Universidade Nova de Lisboa. |
| A Faculdade de Ciências e Tecnologia e a Universidade Nova de Lisboa têm o direito, perpétuo e sem limites geográficos, de arquivar e publicar esta dissertação através de exemplares impressos reproduzidos em papel ou de forma digital, ou por qualquer outro meio conhecido ou que venha a ser inventado, e de a divulgar através de repositórios científicos e de admitir a sua cópia e distribuição com objetivos educacionais ou de investigação, não comerciais, desde que seja dado crédito ao autor e editor. |
| |

Agradecimentos

Gostaria de agradecer à minha orientadora, a Prof. Dra. Elvira Fortunato pela oportunidade de poder trabalhar num tema inovador como este e ao apoio dado na resolução de problemas apresentados durante o desenvolvimento do meu trabalho, à minha segunda orientadora a Dra. Ana Pimentel pela disponibilidade e paciência que teve no esclarecimento de dúvidas que tive ao longo do percurso da minha tese e especialmente no desenvolvimento dos nanofios de prata.

A seguir segue-se um agradecimento especial a todos os que me ajudaram no trabalho laboratorial e no esclarecimento de dúvidas, ao meu colega Dmytro Chervonovskyy que trabalhou nos nanofios comigo, ao Tomás Freire pela sua monitorização contante no primeiro mês da tese, à Eng. Alexandra Gonçalves e Eng. Sónia Pereira por toda ajuda na obtenção dos materiais necessários e no esclarecimento de duvidas laboratoriais assim como no uso dos equipamentos, à Carolina Marques na ajuda necessária com o laser, ao Tomás Calmeiro na sua ajuda com o SEM, AFM e no esclarecimento de duvidas relativas aos mesmos, ao Paul Grey e à Inês Cunha no screen-printing dos elétrodos interdigitais, à Andreia Santos no esclarecimento de duvidas sobre o funcionamento do sensor assim como na ajuda da montagem do equipamento necessário ao seu funcionamento, ao Tiago Carvalho pela sua ajuda no potencióstato durante os testes preliminares feitos ao sensor e finalmente ao Prof. Dr. João Canejo pela enorme ajuda nos testes de compressão do sensor e de tração da nata de coco, assim como no esclarecimentos de duvidas relativas ao assunto.

O maior agradecimento que posso dar vai para a minha família e amigos, que estiveram comigo desde o início, apoiaram-me quando precisei e fizeram-me companhia nos bons e maus momentos destes longos, mas curtos 5 anos.

Resumo

O interesse e a necessidade em sensores de saúde portáteis, confortáveis e duráveis têm aumentado ao longo dos anos, devido à sua praticabilidade e potencial em ajudar as pessoas a monitorizarem os seus sinais vitais. No entanto, a produção de um sensor completamente biodegradável de baixo custo ainda representa um desafio. Por isso, vários tipos de celulose estão a ser usados à nanoescala por preencherem os requisitos necessários com as suas excelentes propriedades, assim como metais como o ouro, prata e cobre, que na forma de nanofios os torna ótimas alternativas como materiais de deteção em sensores de pressão.

Este projeto tem como objetivo desenvolver um sensor de pressão fácil de fabricar, de baixo custo, completamente biodegradável, à base de papel, flexível e de fácil uso em cuidados de saúde. Os nanofios de prata são produzidos pela síntese poliol assistida por micro-ondas e purificados em 3 fases de decantação. O substrato do sensor é criado pressionando a nanocelulose bacteriana da nata de coco. Os elétrodos interdigitais são produzidos na sua superfície por impressão em tela. O papel é revestido com nanofios de prata por imersão, colocado no meio dos elétrodos interdigitais e encapsulado com a nanocellulose bacteriana, concluindo assim a construção do sensor. O sensor apresentou um rápido tempo de resposta de 1.8 ms, um tempo de recuperação de 0.8 ms e uma elevada estabilidade durante 15000 ciclos. Os melhores valores de sensibilidade obtidos foram 12.05 kPa⁻¹ (0.031-1.4 kPa), 4.29 kPa⁻¹ (1.4-2.8 kPa), 1.59 kPa⁻¹ (2.8-5.6 kPa) e 0.38 kPa⁻¹ (5.6-14 kPa) com o sensor a utilizar 6 ciclos de revestimento por imersão no papel Tork. O sensor também conseguiu detetar uma baixa pressão de 31 Pa e apresentou um consumo mínimo e máximo de energia de 3.75×10⁻⁵ W e 1.32×10⁻² W, com uma tensão de trabalho de 2V.

Palavras-chave: nanofios de prata, síntese poliol assistida por micro-ondas, impressão em tela, celulose bacteriana, revestimento por spray, revestimento por imersão, nata de coco, elétrodos interdigitais, papel, sensor, piezoresistivo.

Abstract

The interest and need in portable, comfortable and durable health care sensors have increased along the years, due to their practicability and potential in helping people monitoring their vital signs. However, an all biodegradable low-cost sensor still poses a challenge to fabricate. So, cellulose is being used in the nanoscale form, due to filling all the necessary requirements with their excellent properties. The same can be said for metals like gold, silver and copper, which in the form of nanowires makes them great alternatives as sensing materials for pressure sensors.

This work aims to develop a facile craft, low-cost, completely biodegradable, paper-based flexible and wearable pressure sensor for health care. The AgNWs are produced by the microwave-assisted polyol synthesis and purified with 3 decantation phases. The sensor substrate is made by pressing the bacterial nanocellulose (BNC) of *nata de coco*. The interdigitated electrodes (IDEs) are then screen-printed on its surface. The tissue paper is dip coated with the AgNWs, placed in the middle of the IDEs and encapsulated with the BNC, concluding the sensor construction. The sensor displayed a fast response time of 1.8 ms, a recovery time of 0.8 ms and it also showed high stability during 15000 cycles. The best sensitivity values achieved were 12.05 kPa⁻¹ (0.031-1.4 kPa), 4.29 kPa⁻¹ (1.4-2.8 kPa), 1.59 kPa⁻¹ (2.8-5.6 kPa) and 0.38 kPa⁻¹ (5.6-14 kPa), with the 6 dip coating cycles paper Tork on the sensor. The lowest detectable pressure was 31 Pa and the minimum and maximum energy consumption values recorded were 3.75×10⁻⁵ W and 1.32×10⁻² W with a 2V working voltage.

Keywords: silver nanowires, microwave-assisted polyol synthesis, screen-printing, bacterial cellulose, spray coating, dip coating, nata de coco, interdigitated electrodes, tissue paper, sensor, piezoresistive.

General Index

| Introduction | 1 |
|----------------------------------------------------------------------|----|
| 1.1 Paper: A viable alternative to traditional materials | 1 |
| 1.2 Nanocellulose: Main features and production techniques | 2 |
| 1.3 Silver Nanowires: Properties and production methods | 3 |
| 1.4 Sensors: Performance and transduction mechanisms | 5 |
| Materials and Methods | 6 |
| 2.1 Synthesis and purification of the AgNWs solution | 6 |
| 2.2 Production of the BNC membrane and the interdigitated electrodes | 7 |
| 2.3 Dip and spray coating of the AgNWs on the tissue paper | 7 |
| 2.4 Sensor assembly and performance testing | 7 |
| Results and Discussion | 8 |
| 3.1 Synthesis and purification of the AgNWs solution | 8 |
| 3.1.1 AgNWs Synthesis | 8 |
| 3.1.2 Purification process | 9 |
| 3.2 Production of the BNC membranes | 13 |
| 3.3 Screen printing of the interdigitated electrodes | 15 |
| 3.4 Coating of the tissue paper with AgNWs | 18 |
| 3.4.1 Spray coating | 18 |
| 3.4.2 Dip coating | 19 |
| 3.5 Pressure sensor performance | 21 |
| Conclusion and Future Perspectives | 28 |

| References | 30 |
|------------|----|
| | |
| Annexes | 33 |

Index of Tables

| Table 1.1 - Paper as a sensor substrate in comparison with traditional materials [5]. | 2 |
|---------------------------------------------------------------------------------------------------------------------------------------------------------------------------------------------------------------------------------------------------------------------------------------------------------------------------------------------|------|
| Table 1.2 – Summary of the performance of some flexible and wearable pressure sensors | 5 |
| Table 3.1 – Diameter of some of the wrinkles, pores and fibers present in the nata de coco membrane | .15 |
| Table 3.2 – BNC and PET electrical resistances throughout the folding test. | .17 |
| Table 3.3 – Sheet resistance values of the 10 dip coating cycles done with the OS on both Tork and Kimber paper | - |
| Table 3.4 – Comparison between the currents and their respective pressures of the 2 sensors with 4 dip coat cycles paper Tork, with two different initial currents and the potentiometer at 577 Ω , displayed in Figure 3. | .27. |
| Table 6.1 – Quantities and prices of the products, bought in bulk, used during the fabrication of the necess components to produce the sensor and to fabricate one sensor | - |
| Table 6.2 - Comparison between the currents and their respective pressures of one 5 dip coating cycles partork sample (0.7×0.5 cm), with the potentiometer at 215 Ω , to another 5 dip coating cycles paper Tork sam (0.5×0.5 cm), with the potentiometer at 17.05 k Ω . Their sensitivity plots are displayed in Figure 3.29 | ple |
| Table 6.3 - Comparison between the currents and their respective pressures of the two sensors (sample 1 a sample 2) with 6 dip coating cycles paper Tork, with two different initial currents and the potentiometer at 5 Ω . Their sensitivity results are displayed in Figure 3.30 | 577 |
| Table 6.4 – Paper types used for the dip and spray coating method during the tissue paper coating process. | 39 |
| Table 6.5 – Sensitivity values of each sensor sample tested in the sensitivity tests | .39 |

Index of Figures

| Figure 1.1 - Schematic of a nanocellulose production process with pre-treatment and treatment techniques. [11] |
|--------------------------------------------------------------------------------------------------------------------------------------------------------------------------------------------------------------------------------------------------------------------------------------------------------------------------------------------------------------------------------------------------------------------------------------------|
| Figure 1.2 - SEM images of the surface morphology of AgNWs-coated fabric (a-d) with different AgNWs positions, in which (c) is the SEM image of the AgNWs between the yarns and (d) the AgNWs coated on the single fiber [16] |
| Figure 1.3 - Scheme of the polyol process divided into 4 steps used to synthesize the AgNWs. [23]4 |
| Figure 3.1 –The images show the AgNWs solution appearance during its synthesis at the ending of each stage. (a) AgNO ₃ and EG are stirred for 8 min at 700 rpm; (b) NaCl and EG are added to the mixture and stirred for 12 min at 1000 rpm; (c) the solution in the previous stage is added to a solution of PVP and EG drop by drop and stirred for 5 min at 1000 rpm; (d) oxidised solution; (e) good quality AgNWs solution |
| Figure 3.2 – Solution appearance after the microwave synthesis. (a) oxidised solution; (b) SS solution; (c) OS solution; (d-f) respective optical microscope images after the purification process |
| Figure 3.3 – The (A) pair of solutions was decanted with 30 ml of acetone and the (B) pair by 35 ml. The (C) pair of solutions which were oxidised was decanted by 35 ml of acetone. Image (D) shows a close up of the two phases formed after the decantation process is complete |
| Figure 3.4 – (a) AgNWs remaining after the acetone decantation; (b) phase separation of the AgNWs (silver stream) from the supernatant (yellow solution) during the methanol decantation; (c) AgNWs remaining after the methanol decantation and the supernatant removal; (d) AgNWs remaining after the final decantation of acetone and IPA. |
| Figure 3.5 – Comparison between two optical microscope images of solutions synthesized through the SS, with the same purification process, but with different results. |
| Figure 3.6 – SEM images comparing the commercial AgNWs with the ones produced using the OS. (a) AgNWs after the first purification (acetone decantation); (b) AgNWs after the final purification (acetone and IPA decantation); (c) the presence of other by-products even after the final purification; (d-f) commercial AgNWs with different magnifications. |
| Figure 3.7 – (a) XRD analysis results of 4 different samples. (b) UV-Vis absorption spectrum analysis of 4 different samples with their respective peaks and shoulders |

| Figure 3.8 – (a) Manual press of the nata de coco cubes; (b) the resulting wet membrane after the manual press; (c) membrane after drying in a vacuum desiccator; (d) membrane after the hydraulic press |
|-------------------------------------------------------------------------------------------------------------------------------------------------------------------------------------------------------------------------------------------------------------------------|
| Figure 3.9 – Stress-Strain $(\sigma$ - $\varepsilon)$ plots of the dry <i>nata de coco</i> membrane (a) and the two membranes glued together (b). |
| Figure 3.10 – (a) SEM images of a dry membrane wrinkles produced when it shrunk during the drying process; (b) the Acetobacter xylinum bacteria (red circle); (c) the BNC fibers appearance with their random network pattern |
| Figure 3.11 – Materials and method used to fabricate the IDEs on the membrane surface and the resulting product |
| Figure 3.12 – Optical stereo microscope and SEM images of the IDEs and their respective finger electrodes printed on both BNC and PET substrates |
| Figure 3.13 – Folding test damage on the structural state of the BNC and PET substrates before and after 24 hours |
| Figure 3.14 - SEM images of the finger electrodes appearance on both PET and BNC substrates after the folding test |
| Figure 3.15 – 5 ml of AgNWs diluted in 10 ml of IPA (a) airbrush XL2000, (b) no solution sprayed, (c) half flask (7.5 ml sprayed), (d) full flask (15 ml sprayed) |
| Figure 3.16 – 15 ml sprayed. (a) 1 ml of AgNWs diluted in 14 ml of IPA, (b) 3 ml of AgNWs diluted in 12 ml of IPA |
| Figure 3.17 – SEM images in different magnifications of the Paper Whatman grade 2 spray coated with 3 ml of the conductive SS solution diluted in 12 ml of IPA |
| Figure 3.18 – The dip coating process on the paper Tork and its appearance with the AgNWs before and after annealing |
| Figure 3.19 – Physical appearance of both Kimberly and Tork papers (already dry) throughout 10 dip coating cycles |
| Figure 3.20 – Hitachi Tabletop SEM (with a filter that highlights the contrast between the zones with high and low AgNWs density) images of the paper Tork with 0,1,2,4,5,6,8 and 10 dip coating cycles with the OS AgNWs solution. |
| Figure 3.21 – (a) sensor not encapsulated with the BNC membrane. View of the encapsulated sensor from the front (c,d) and back (b,e). (b-c) in natural light with copper strips attached, (d-e) without copper strips in artificial white light. |
| Figure 3.22 – Current-time plots of different pressures and pressure durations applied by a finger (so the pressure values couldn't be measured) to the paper Tork sensor $(0.7\times0.5 \text{ cm})$ with 5 dip coating cycles and the potentiometer at 571 Ω . |
| Figure 3.23 – Response and recovery times of a fast-medium pressure (images on the first row) and a prolonged heavy pressure (images on the second row) applied by a finger on the paper Tork with 5 dip coating cycles. |

| Figure 3.24 – Response and recovery times of the sensor with 4 and 6 dip coating cycles under different pressures and pressure durations applied by a finger (so the pressure values couldn't be measured) with the potentiometer at 571Ω . |
|------------------------------------------------------------------------------------------------------------------------------------------------------------------------------------------------------------------------------------------------------------------------------------------------------------------------------------------------------------------------------------------------------------------------------------------------------------------------------------------------------|
| Figure 3.25 – Machine with Arduino Uno and setup used to perform the stability test to determine the sensor stability |
| Figure 3.26 – Stability test performed on the sensor with the 5 dip coating cycles paper Tork. Image (a) shows the stability results of the full 15000 cycles test. (b) results of the sensor in its correct/initial position. (c) results of the sensor, with the pressure applied in a different location, due to a change in the sensor position, caused by the machine over a period of time. (d) results of the sensor under different pressures, at different times during the stability test. |
| Figure 3.27 – Sensitivity test done on two sensors with 4 dip coating cycles paper Tork, with the potentiometer at 577Ω |
| Figure $3.28 - (a)$ Sensitivity test done on the sensor with the 5 dip coating cycles paper Tork $(0.7 \times 0.5 \text{ cm})$ and the potentiometer at 577 Ω . (b) The compression/deformation of the sensor to the applied force during the test. |
| Figure 3.29 – Sensitivity tests done on the sensor. (a) On the 5 cycles paper Tork (0.7×0.5 cm), with the potentiometer at 215 Ω . (b) On the 5 cycles paper Tork (0.5×0.5 cm), with the potentiometer at 17.05 k Ω 26 |
| Figure 3.30 – Sensitivity test done on two sensors with 6 dip coating cycles paper Tork and the potentiometer at 577 Ω . |
| Figure 6.1 – Spray coating process on a glass substrate and measuring of its electrical resistance with a multimeter |
| Figure 6.2 – Laser welding of the paper Whatman coated with 3 ml of the AgNWs solution produced with the SS. (a,d) paper Whatman without welding; (b,e) welding with 5 watts and 0.762 m/s; (c,f) welding with 6.5 watts and 1.016 m/s. |
| Figure 6.3 - SEM images of the paper Tork coated with AgNWs from an OS solution, each image shows the increase in the NWs coverage with each dip coating cycle. The images correspond respectively to 4,6,8,10 cycles (left to right). |
| Figure 6.4 – SEM images with the SEM-FIB (no filter) and Hitachi Tabletop SEM (filter that highlights the contrast areas with high and low AgNWs density) of the Kimberly paper with 10 dip coating cycles, fully covered with AgNWs of the OS, exhibiting a resistance of $6.35\pm3.04~\mathrm{k}\Omega/\mathrm{sq}$. |
| Figure 6.5 – XRD analysis of the n <i>ata de coco</i> membrane, which exibits 3 characteristic peaks at 14.5°, 16.7° and 22.7° |
| Figure 6.6 – FTIR analysis of the transmittance and absorbance spectre of two <i>nata de coco</i> membrane samples |
| Figure 6.7 – AFM 3D morphological images of the membrane surface through the use of the Gwyddion software |
| Figure 6.8 - AFM 3D morphological images of the finger electrodes surface through the use of the Gwyddion software |
| Figure 6.9 – Setup (sensor, probes and the KEYSIGHT 33500B series waveform generator) with the weights used during the sensitivity tests to apply specific pressures on the sensor |

| Figure 6.10 - Compression machine applying pressure on the glass on top of the sensor, while the probes apply |
|-----------------------------------------------------------------------------------------------------------------------------------------------------------------------------------------------------------------------------------------------------------------------|
| the voltage supplied by the KEYSIGHT 33500B series waveform generator, to the interdigitated electrodes |
| pads |
| Figure 6.11 - Current-Voltage-Pressure plot of the 5 dip coating cycles paper Tork $(0.5\times0.5 \text{ cm})$ with the potentiometer at $17.05 \text{ k}\Omega$, with the respective sensitivity results displayed on Figure 3.29 and the exact values on Table 6.2 |
| |
| Figure 6.12 – High quality SEM images of the OS solution used to measure the AgNWs dimensions. (a) |
| AgNWs after the first purification (acetone decantation); (b) AgNWs after the final purification (acetone and |
| IPA decantation)40 |

List of Abbreviations and Acronyms

NC Nanocellulose

CNC Cellulose Nanocrystals **NFC** Nanofibrillated Cellulose **Bacterial Nanocellulose BNC** BC **Bacterial Cellulose NDC** Nata de Coco

TS Tensile Strength

Ultimate Tensile Strength **UTS**

AgNWs Silver Nanowires **AgNPs** Silver Nanoparticles OS **Optimised Synthesis** SS Standard Synthesis **TCEs** Conductive Electrodes Indium Tin Oxide ITO **MTFs** Metal Thin Films **PVP** Polyvinylpyrrolidone Ethylene Glycol EG **AuNWs** Gold Nanowires Isopropyl Alcohol **IPA** Indium Tin Oxide ITO Interdigitated Electrodes **IDEs**

Scanning Electron Microscope **SEM** X-Ray Powder Diffraction **XRD** Atomic Force Microscopy **AFM** Polyethylene Terephthalate **PET WHC** Water Holding Capacity Moisture Retention Capacity **MRC**



List of Symbols

 $\begin{array}{ccc} \sigma & & \text{Stress} \\ F & & \text{Force} \end{array}$

t Sample thickness W Sample width

ε Strain

Sample length L \mathbf{E} Young's modulus $\mathbf{R}_{\mathbf{S}}$ Sheet resistance \mathbf{R} Resistance Resistivity ρ V Voltage I Current \mathbf{S} Sensitivity P Pressure

C Solution concentration
 m Mass of the solute dissolved
 V Total volume of the solution

CrI Crystalline index

Motivation

New types of sensors especially health care sensors are being manufactured for every task imaginable. In order to keep up with the constant requirements and regulations impose on them, other less then obvious materials are being tested to substitute the traditional materials that are now falling behind. These alternative materials need to be cheap, abundant, flexible and more importantly biodegradable.

Today we can find pressure sensors for healthcare in the form of E-textiles, head/wrist mounted devices and skin sensors. These can be capacitive, piezoelectric or piezoresistive and each has a different transduction mechanism and material combinations for their structure. However, there are still too few sensors which are completely biodegradable, low-cost and of facile craft. Certain materials like cellulose and metals like gold and silver, which have been used and are still now in many applications due to their excellent properties, are being made in the form of several nanostructures to enhance their properties and sometimes discoverer new and unique ones, which display interesting effects during their application on many devices as for example substrates or sensing materials for pressure sensors.

This work aims to develop a facile craft, low-cost, completely biodegradable, paper-based flexible and wearable pressure sensor for health care, to help the environment and people with limited income, in isolated places to be able to receive or buy this sensor and monitor their vital signs. In order to do so, the AgNWs are produced by the microwave-assisted polyol synthesis, which is the only method in this work that uses expensive equipment, when compared to others used throughout the construction of the sensor. However, this enables a very fast synthesis with a better purified solution, when compared to other methods. The sensor substrate is made with BNC from *nata de coco*, which is a very cheap and abundant Philippines desert, produced by a bacterium called Komagataeibacter xylinus (also known as Acetobacter xylinum) that ferments the coconut water, using it as a carbon source. The interdigitated electrodes (IDEs) are screen-printed on the substrate surface and the tissue paper is dip coated with the AgNWs. This is finalised by assembling all the components into a finished pressure sensor, which stands out from other sensors.



1

Introduction

The interest and need in portable, comfortable and durable health care sensors, has increased along the years, due to their practicability and potential in helping people monitoring their vital signs. Wearable devices which are capable of information gathering, processing, communication and power supply, are very useful to people with certain diseases in need of constant supervision. Today we can find sensors for healthcare in the form of E-textiles, head/wrist mounted devices and skin sensors. The fabrication of skin sensors has been in development for some years, resulting in the already existence of various sensor types and material combinations for their structure, although an all biodegradable low-cost sensor still poses a challenge to fabricate. Certain materials like cellulose, display several unique properties and structures in their bulk form, however, at the nanoscale, even their behaviour to external stimulations may change, being greatly enhance in every aspect and making excellent substrates for sensors. The same can be said for metals like gold, silver and copper, which in the form of nanowires makes them great alternatives as sensing materials for pressure sensors.

1.1 Paper: A viable alternative to traditional materials

Cellulose is the most abundant organic polymer on Earth and is the main material of which paper is made. It can be extracted from lignocellulosic biomass, which is present in wood pulp and plant fiber, and its cell wall structure consists of 35-50% cellulose [1]. The steps involved in the manufacturing of pulp and paper are raw material preparation (chipping and debarking), mechanical or chemical pulping, chemical recovery, mechanical or chemical bleaching, stock preparation and finally by dewatering, pressing and drying, the paper production process is complete [2]. Paper has various properties like, excellent flexibility, a three-dimensional fibrous structure, good price, renewability, almost endless supply, large quantities obtained with low cost processes, high porosity, biodegradability and excellent mechanical performance. Traditional materials like glass, silicon, PDMS, PEN, PET and Polyamide, suffer from many manufacturing, economic and environmental problems. So, paper is seen as a viable candidate to substitute these materials on many devices and their applications, especially as a substrate [3][4]. However, paper also has some properties which can make its application on certain devices, like a sensor, a problem, being two of them, the absorption of moisture and its retention, which can happen upon contact with sweat, when placed on the skin. Also, if a specific electrical resistance value is desired throughout the entirety of the paper, this can be difficult to obtain, due to

its non-homogeneity and high porosity. On Table 1.1 are shown some properties of paper, in comparison with other materials, when is used as a sensor substrate.

Table 1.1 - Paper as a sensor substrate in comparison with traditional materials [5].

| Property | Material | | | | | |
|-----------------------------|-----------|-----------|----------------|---------------|-------------------|------------------|
| Troperty | Glass | Silicon | PDMS | PET/PEN | Polyamide | Paper |
| Surface profile | Very low | Very low | Very low | Low | Moderate | Moderate |
| Flexibility | No | No | Yes | Yes | Yes | Yes |
| Structure | Solid | Solid | Solid | Solid | Fibrous | Fibrous |
| Surface-to-volume ratio | Low | Low | Low | Low | Moderate | High |
| Fluid flow | Forced | Forced | Forced | Forced | Absorption | Capillary action |
| Sensitivity to moisture | No | No | No | No | To some extent | Yes |
| Biocompatibility | Yes | Yes | Yes | Yes | Limited | Yes |
| Disposability | No | No | No | No/Recyclable | No/Recyclable | Yes |
| Biodegradability | No | No | To some extent | No | No | Yes |
| High-throughput fabrication | Yes | Yes | No | Yes | Yes | Yes |
| Functionalization | Difficult | Moderate | Difficult | Easy | Easy | Easy |
| Spatial resolution | High | Very high | High | High | Moderate | Low to moderate |
| Homogeneity of the material | Yes | Yes | Yes | Yes | No | No |
| Price | Moderate | High | Moderate | Moderate | More than PET/PEN | Low |
| Initial investment | Moderate | High | Moderate | Moderate | More than PET/PEN | Low |

1.2 Nanocellulose: Main features and production techniques

A single cellulose fiber is made up of groups of microfibers, with a diameter around 20–35 µm and in turn, the microfibers are composed of nanofibers bundles. Nanocellulose (NC) fibers measure less than 100 nm in diameter and several micrometers in length, its low density is around 1.6g/cm³, it can have 220 GPa of elastic modulus, a tensile strength that can reach up to 10 GPa and excellent optical transparency. NC paper possesses all the properties of normal cellulose paper but greatly enhanced, due to their 1D structure and high surface areas. NC can be divided in three types, cellulose nanocrystals (CNC), nanofibrillated cellulose (NFC) and bacterial nanocellulose (BNC). Each have a different fiber structure, but even considering two fibers of the same type, their properties and dimensions greatly depend on their source of raw material, pre-treatment technique to form the cellulose microfibril and the treatment technique used to finally form the NC fiber [1][6].

BNC is produced by placing a bacterial cellulose strain such as Komagataeibacter xylinus, Acetobacter xylinum or Gluconacetobacter xylinus in a solution with various nutrients and glucose as a carbon source. This will produce a highly hydrated white NC which will be submitted to a purification process and then mechanical treatment. Compared to CNC and NFC, BNC has better purity, crystallinity and mechanical stability, it's also capable of reaching a Young's modulus around 114 GPa. NFC is extracted by means of mechanical-chemical treatment of wood-based cellulose, it has high tensile strength, high aspect ratio, capable of reaching a Young's modulus around 100 GPa, low thermal expansion and exhibits an oxygen barrier and a web like structure. CNC possesses a rod-like structure and is made by simply removing the amorphous regions from cellulose with acid hydrolysis, leaving the crystalline region intact, it has a large surface area, excellent stability, Young's modulus around 206 GPa and exceptional optical properties. Various treatment techniques exist to turn purified

cellulose into NC, the majority of them are either mechanical or chemical. The mechanical techniques consist of defibrillating the cellulose through mechanical forces while, the chemical techniques use chemical agents to degrade the cellulose, leading to the production of NC [7]–[10]. Figure 1.1 bellow shows a schematic of a NC production process.

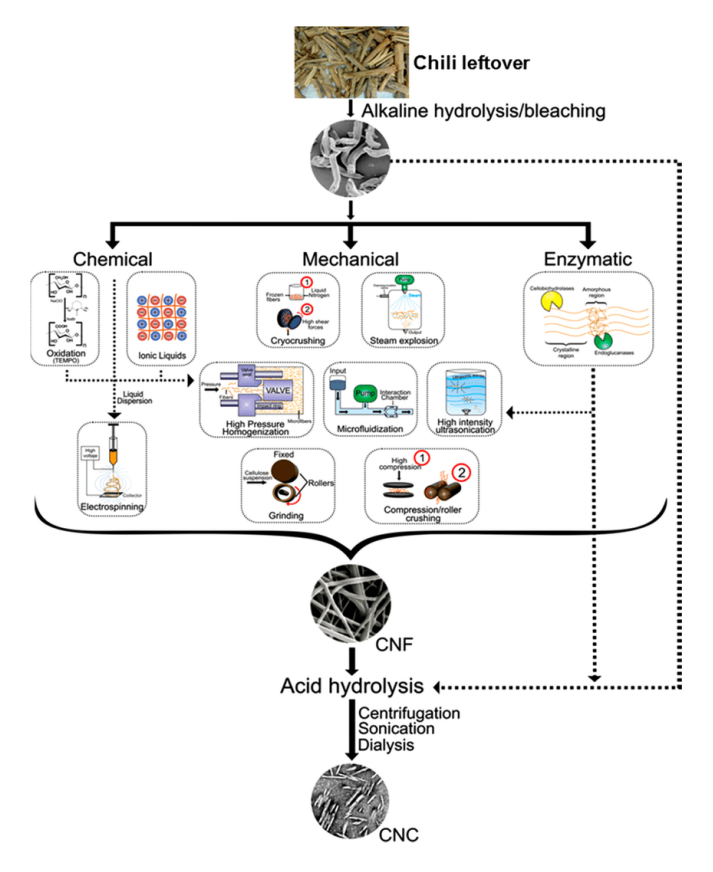


Figure 1.1 - Schematic of a nanocellulose production process with pre-treatment and treatment techniques. [11]

Nata de coco (NDC) is the source of the BNC used in this work, which is a Philippines desert, produced by a bacterium called Komagataeibacter xylinus (also known as Acetobacter xylinum) that ferments the coconut water, using it as a carbon source. The BNC created is free of non-cellulosic products and has a high purity [12][13]. In the work of Handika Dany Rahmayanti et al. (2019), the physical and mechanical properties of six brands of *nata de coco were* studied, the tensile strength (TS) was in the ranged of 0.12–0.41MPa, the Young's modulus was between 3–18.47MPa and the transmittance was 38–75% [14].

1.3 Silver Nanowires: Properties and production methods

The importance in finding materials to ensure excellent mechanical and electrical properties for all components in flexible and wearable devices keeps raising with the increasing demand for health care sensors. Traditional components like transparent conductive electrodes (TCEs) based on indium tin oxide (ITO) or metal thin films (MTFs), have high processing costs, limited flexibility, material scarcity and brittleness. AgNWs however don't suffer from those problems, they have a one-dimensional structure, a simple and low-cost synthesis via the polyol method and a number of exciting properties, which are not exhibited by their bulk form and so, they are considered a viable alternative candidate [15]–[17]. Silver has the highest electrical and

thermal conductivity of all the metals and as such, so does the AgNWs when compared to others. It also possesses a surface plasmon resonance, high chemical stability and good mechanical properties such as 2.64GPa of yield strength (σ_y) and 4.84GPa of ultimate tensile strength (UTS) [18]–[20]. Although AgNWs have a lot of good properties due to their high surface-area-to-volume ratio and their structure being multitwinned, corrosion and degradation of their structure is a constant problem, which starts around six months when exposed to the atmosphere [16][21]. Figure 1.2 shows an example of the AgNWs appearance, when coated in the surface of some fabric.

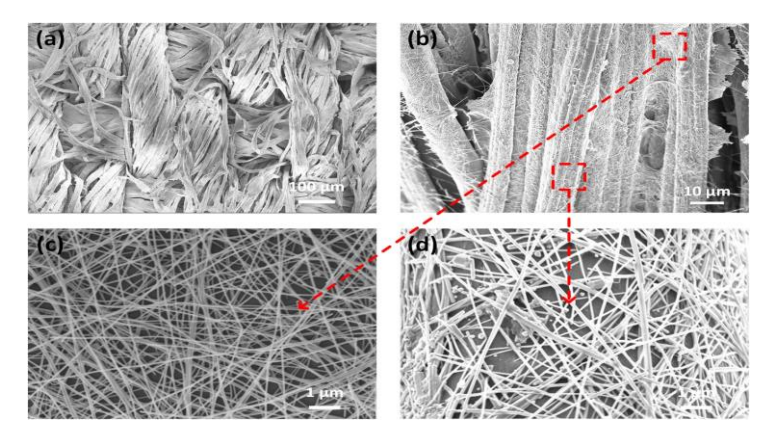


Figure 1.2 - SEM images of the surface morphology of AgNWs-coated fabric (a-d) with different AgNWs positions, in which (c) is the SEM image of the AgNWs between the yarns and (d) the AgNWs coated on the single fiber [16]

There're various AgNWs synthesis methods, but the most widely used is the polyol method. This method uses a metal salt, like silver nitrate (AgNO₃), that will be reduced through the use of ethylene glycol (EG), which will also act as the solvent of the solution. Polyvinylpyrrolidone (PVP) is than used as a capping agent to prevent aggregation and control the growth direction of the AgNWs. Sodium chloride (NaCl) is added to control the reaction rate and will act as the nucleating agent [22], however, ferric chloride (FeCl₃), a mix of potassium bromide (KBr) or sodium bromide (NaBr) can also be used as replacements, but will produce different results during the AgNWs production. Figure 1.3 bellow shows the growth process of an AgNW.

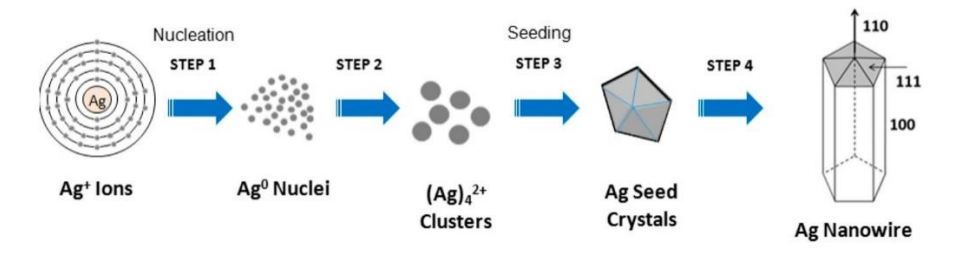


Figure 1.3 - Scheme of the polyol process divided into 4 steps used to synthesize the AgNWs. [23]

The AgNWs needs temperatures around 160-170 °C in order to be formed and this can be done by conventional heating in an oven or by microwave-radiation [22]. The method chosen in this work to synthesize the AgNWs was the microwave-assisted polyol method, due to its huge increase in reaction rate, product yields and purity, when compared to conventional heating. This happens because the microwave radiation creates an electromagnetic field which causes the molecules with a dipolar structure, those being EG and PVP, to oscillate, creating friction between them and producing heat. Furthermore, the field created also helps in the one directional growth of the AgNWs process, by aligning the AgNO₃ molecules [24][25]. A detailed study of how the various synthesis parameters affect the AgNWs growth and dimensions can be found at Sahin Coskun et al. (2011) [22] and at Zao Yi et al. (2017) [26].

1.4 Sensors: Performance and transduction mechanisms

Pressure sensors can be built by using various materials, however, depending on those materials, the sensor may operate with a different transduction mechanism. Crystalline materials, which have the piezoelectric effect, generate internal electrical charge created from an applied mechanical stress, changing the material shape. Capacitive pressure sensors, measure changes in electrical capacitance, caused by the movement of one of the conductive plates that acts as the diaphragm, when moved by an applied pressure. The piezoresistive effect, consists in the change of electrical resistivity of the material, when subjected to deformation of its initial configuration. The piezoresistive sensors have the advantage of being easy to build, low energy consumption, shielded from radio-frequency noise and have very high sensitivity values [27]. The most important parameters to consider, when making a pressure sensor are the sensitivity (S), the response and recovery times, and the sensor stability. The sensor sensitivity is determined by using the equation (1.1) and is defined as the slope of the output characteristic curve, which translates to how much output change the sensor provides for a given change in applied pressure, the higher the output, the higher the sensitivity value. The sensor response and recovery times are the amount of time required for the sensor to read the stimulus and then return to its original state. Finally, the sensor stability provides information regarding the number of input stimulus necessary for the sensor to begin producing a significant deviation of the respective output signal.

$$S = (\Delta I/I_0)/\Delta P$$
 equation (1.1)

When a fixed voltage is applied to the piezoresistive sensor, ΔI (mA) is the relative change in current produced by applying pressure on the sensor. I_0 (mA) is the constant initial current created by the encapsulation pressure of the sensor. ΔP (kPa) is the change in applied pressure. **S** (kPa⁻¹) is the sensitivity already described above [28]. Table 1.2 bellow shows the performance summary of some flexible and wearable pressure sensors.

| Pressure Sensor | Sensor Type | Energy consumption (W) | Sensitivity (kPa ⁻¹) | Working voltage (V) | Detection Range (Pa) | Response Recovery (ms) | Loading Unloading cycles |
|--------------------------------------------------------------------|------------------------------|---------------------------|---------------------------------------------------------|------------------------|---------------------------------|---------------------------|-----------------------------|
| Tissue Paper/AuNWs [28] | Piezoresistive | 3×10 ⁻⁵ | 1.14 | 1.5 | 13-50000 | 17 | 50000 (2.5 kPa) 2Hz |
| APBP Tissue Paper with AgNWs [29] | Piezoresistive | 10-8 | 1.5 | 0.1 | 30-30247 | 90/90 | / |
| AgNWs/PDMS with Multiscale Structure [30] | Capacitive | / | 3.8 0.8 0.35 | / | 15-500 500-2500 2500-4500 | 150/150 | 5000 (1.5 kPa) |
| Single wall nanotube into tissue paper [31] | Piezoresistive | 10 -6 | 2.2 1.3 | 0.1 | 35-2500 2500-11700 | 40 | / |
| HPM-PDMS/MWCNT composite films. [32] | Piezoresistive | / | 83.9 0.4 | 0.1 | 0.5-140 140-10000 | 90/170 | 29000 (4 kPa) 1Hz |
| Cotton fibers/AgNWs [33] | Piezoresistive | / | 3.4 | / | 0-1000 | 50/50 | 5000 (0.1 kPa) 1Hz |
| Microstructures of Polypyrrole Films [34] | Piezoresistive | / | 19.32 (<250 Pa) 0.51 (>850 Pa) | 1 | 1-2000 | 20/30 | 1000 (0.673 kPa) |
| Polystyrene beads pyramid-shaped PDMS [35] | Capacitive Piezoresistive | / | 44.5 (<100 Pa) 449 (<10 Pa) 2.7 (>300 Pa) | / | 0.14-35000 0.14-600 | 50/100 9/30 | 5000 (400 Pa) |
| PDMS pyramid microstructure and walled nanotube network [36] | Piezoresistive | 26.4×10 ⁻⁹ | 2760 (<400 Pa) 8656 (400-900 Pa) 1874.5 (>900 Pa) | 30 | 7.3-1200 | 4 | 10000 |

 $Table \ 1.2-Summary \ of the \ performance \ of some \ flexible \ and \ we arable \ pressure \ sensors.$

Most pressure sensors have a very long duration time, especially the piezoresistive ones and every sensor displayed on Table 1.2 has the capacity to monitor the heart rate, which in a normal person beats one time every 600-1000 ms. A more conductive sensing material will improve the sensor response/recovery time and its sensitivity values due to producing higher ΔI for the same pressure, however, it will also increase its energy consumption. So, the sensor sensitivity, will be higher the lower the established I_0 and the higher the ΔI value.

2

Materials and Methods

2.1 Synthesis and purification of the AgNWs solution

The synthesis and purification of the AgNWs produced in this work is based on the knowledge already developed from other master thesis and further optimised. The microwave-assisted polyol synthesis process begins by first producing a solution, Sol (A), with 50 ml of ethylene glycol (EG, LABKEM) and 0.05g of sodium chloride (NaCl, PanReac Quimica), which is stirred at 800 rpm until complete dissolution. Another solution, Sol (B), is prepared with 100 ml of EG and 1.0 g of polyvinylpyrrolidone (PVP, Sigma-Aldrich) and left at 160 °C and 800 rpm until full dissolution. Sol (C) is made by adding 0.09 g of silver nitrate (AgNO₃, Honeywell) in an Erlenmeyer flask with 5 ml of EG and stirring it at 700 rpm for 8 min. Then 5 ml of Sol (A) is added to Sol (C) and stirred at 1000 rpm for 12 min. Finally, 7.5 ml of Sol (B) is transferred into an Erlenmeyer flask and all the solution in the other Erlenmeyer flask (Sol (A) + Sol (C)) is added drop by drop to Sol (B) and stirred for 5 min at 1000 rpm. The solution is poured into a microwave tube and then placed in a CEM Discover SP - microwave synthesizer at 190 °C, 200 W and 250 Psi for 10 min.

The solution is retrieved from the microwave and placed into an ultrasonic bath for 15 min at 50 °C to disperse any nanowires or nanoparticles aggregates. After that, the solution is divided into two 50 ml centrifuge tubes, 30 ml of acetone are added to both tubes and the solution is left to precipitate for 1h. The supernatant is then removed with a pipette and 15 ml of methanol are added to the nanowire precipitate. The tubes are placed in an ultrasonic bath to disaggregate the nanostructures followed by a centrifugation at 2000 rpm for 30 minutes. The supernatant is thrown away, 10 ml of IPA and 20 ml of acetone are poured into the two tubes and the solution is agitated by hand to avoid over-exposure of the AgNWs to the ultrasonic bath which might cause them multiple fractures. The solution is then placed 30 min in a centrifuge at 2000 rpm and the supernatant is removed at the end. To conclude the AgNWs are dispersed in 5 ml of IPA and then submitted to SEM, XRD and UV-Vis spectroscopy. The AgNWs solution was deposited on a silicon wafer and analysed with a Tabletop microscope TM3030 Plus Hitachi and a Scanning Electron Microscopy Focused Ion Beam (SEM-FIB) workstation to observe the sample morphology and its composition. The AgNWs were analysed in an X-ray diffraction - PANalytical Xpert PRO in order to determine the crystallographic structure of the sample, the anode material used was copper and the scan range was 10° to 90°. A Spectrometer UV-Vis_NIR - Perkin Elmer Lambda 950 was used to measure how much the AgNWs solution absorbs/transmits/reflects light, the wavelength used was 200 nm to 700 nm with the solutions in various concentrations.

2.2 Production of the BNC membrane and the interdigitated electrodes

The sugar-free cubes of *nata de coco*, are pressed for 15 minutes with a manual press (HeatPressUK, Swing-a-way) and dried in a vacuum desiccator at 30 °C. Then by using a Manual Hydraulic Press (Specac, 15-ton max.) they are submitted to 10-tons for 5 minutes. The deposition of the interdigitated electrodes (IDEs) is made by screen-printing, with the use of a specific mesh and a Coates Screen Inks - CRSN2442 conductive silver ink. The substrate is placed beneath the mesh attached with Kapton tape, the silver ink on top and the squeegee is moved across the mesh with small pressure to fill the open mesh apertures with ink. Then the substrate is removed and placed on a hotplate attached with the tape for 10 min at 105 °C to dry the electrodes.

2.3 Dip and spray coating of the AgNWs on the tissue paper

In the dip coating method, the AgNWs solution is poured into a small flask, the tissue paper is held by a tweezer and dipped in the solution for 30 seconds. Then the tissue paper is slowly pulled and placed on a hotplate for 10 min at 100 °C until the solvent evaporates. This process is repeated until the resistance desired is achieved. For the final cycle an annealing process is performed for 30 min at 100 °C and then the AgNWs paper is placed in a petri dish to stabilize for 1 day. For the spray coating method, the AgNWs solution is diluted in IPA so the spray coating on the tissue paper can be performed multiple times without any excessive solution waste due to the sensitivity of the process and to minimise any deposition errors. The tissue paper is fixed with Kapton tape on a hotplate, a XL2000 airbrush is filled with the diluted solution and attached to a nitrogen supply with a pressure of 0.5 bar. The airbrush is held at a height of 10 cm from the paper, which is being annealed at 100 °C. The solution is then continuously sprayed on the paper and its resistance measured with a multimeter until a desired value is achieved. Finally, the paper is annealed for 30 min at 100 °C.

2.4 Sensor assembly and performance testing

For the sensor assembly, the AgNWs paper is placed in the middle of the interdigitated electrodes and encapsulated with an BNC membrane. After the assembly, a potentiometer is placed in series with the sensor to function as an auxiliary resistance. The results are recorded on a Tektronix TBS 1000C series digital oscilloscope with a high voltage of 2V from a KEYSIGHT 33500B series waveform generator. In order to determine the sensor performance, it needs to be submitted to various tests. In the first test, the sensor is pressed with different forces and force durations to see how well the sensor can differentiate and react to various human mechanical stimulus, but also to determine its average response and recovery times. The second test, which is the stability test, is done to determine if the sensor is stable during a certain number of input mechanical stimulus and to do this, a unique machine is used and programmed with Arduino UNO to hit the sensor with a specific force at 1 Hz. The final test is done to determine the sensor sensitivity and for this, various weights are placed on top of the sensor to produce an output for each pressure, however, to obtain more accurate results a compression/traction machine is used, which enables the application of an exact desired force with minimum equilibrium error caused by the uneven surface of the sensor. The results are then processed and plotted on various graphs in order to determine the desired parameters values that define the sensor performance.

3

Results and Discussion

3.1 Synthesis and purification of the AgNWs solution

The synthesis chosen for the production of the AgNWs was the microwave-assisted polyol synthesis and the production was divided into two parts, the synthesis and the purification process. The synthesis process was reported as already optimized from previous works, so the majority of the time reserved for the production was spent on the purification process. However, during the tissue paper coating process with the AgNWs, the solution made by using the advised synthesis or standard synthesis (SS) was inefficient and didn't have the necessary quality to be able to create a conductive tissue paper, so an optimised synthesis (OS) was created. The respective results of the SS and OS synthesis will be displayed and compared in detail on this chapter.

3.1.1 AgNWs Synthesis

The polyol method although simple and low cost, has a number of sensible parameters: the heating temperature of the solution, injection rate, stirring rate, PVP:AgNO₃ molar ratio and NaCl quantity. The smallest parameter value variation can impact the quality of the AgNWs produced [22]. Figure 3.1 shows the AgNWs solution appearance during its synthesis at the ending of each stage.

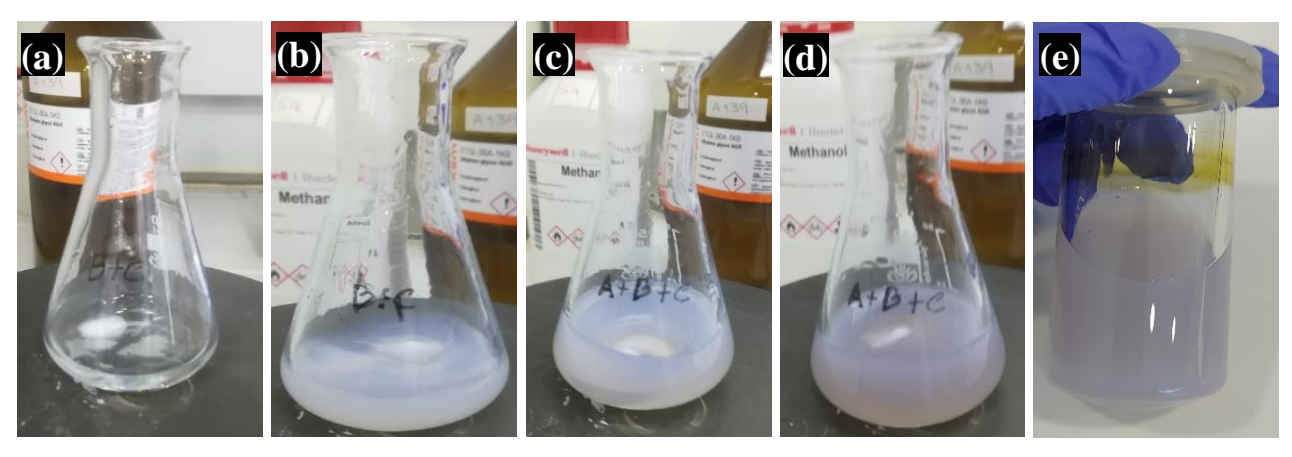


Figure 3.1 –The images show the AgNWs solution appearance during its synthesis at the ending of each stage. (a) AgNO₃ and EG are stirred for 8 min at 700 rpm; (b) NaCl and EG are added to the mixture and stirred for 12 min at 1000 rpm; (c) the solution in the previous stage is added to a solution of PVP and EG drop by drop and stirred for 5 min at 1000 rpm; (d) oxidised solution; (e) good quality AgNWs solution.

A successful AgNWs solution before being placed into the microwave system must have a pearl white purplish colour. The wrong temperature or stirring rate may cause the solution to become transparent with most of the reagents undissolved, resulting in the production of by-products and other nanostructures. Another problem that might occur during synthesis is oxidation. This can happen due to the presence of water, the over exposure of the solution to the atmosphere during its preparation and over-heating the PVP during its dissolution in EG. The last one will cause a change of colour in the solution from transparent to yellow. The solution oxidation was the most prominent problem during synthesis and if carried to the microwave, only NPs will be produced. Figure 3.2 shows the appearance of an oxidise solution compared to a successful SS and OS.

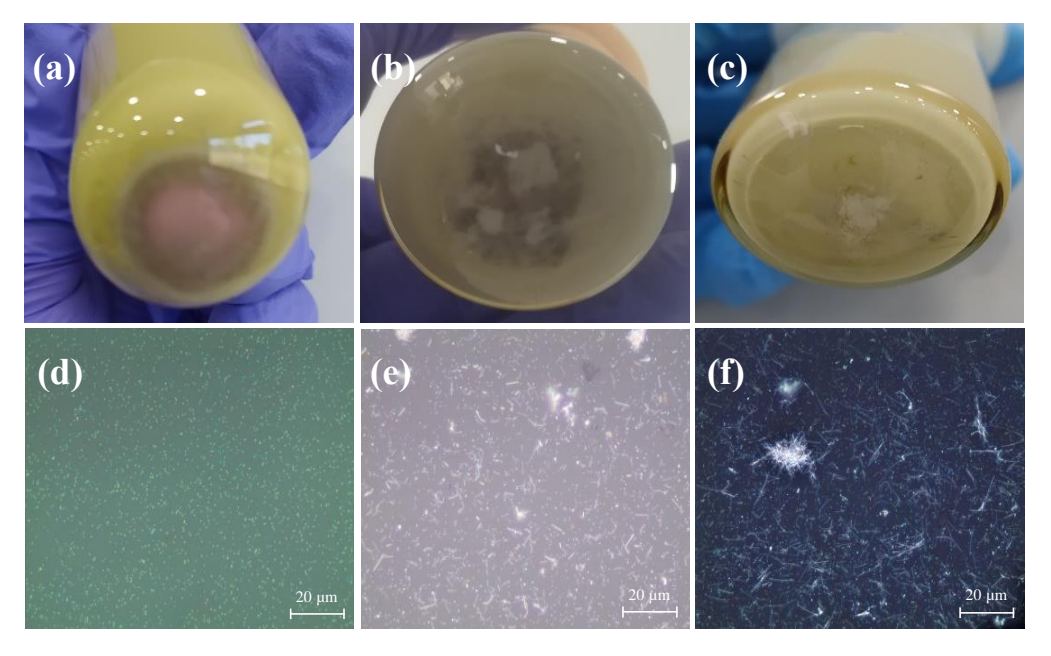


Figure 3.2 – Solution appearance after the microwave synthesis. (a) oxidised solution; (b) SS solution; (c) OS solution; (d-f) respective optical microscope images after the purification process.

The difference between each solution can be seen quite clearly from their quality and appearance in the images of Figure 3.2. The oxidise solution has the presence of a reddish coloured substance at the bottom and was only able to produce nanoparticles. The different results obtained in this phase with the SS and the OS are due to the quantity used of the solution containing 100 ml of EG and 1.0 g of PVP, SS uses 10 ml while OS only uses 7.5 ml. This small change had a great impact in the AgNWs produced. The OS solution produced bigger and more nanowires than the SS, while also having less nanoparticles and PVP remains. If the latter is still present in the solution in large quantity and coated in the nanowires, their conductivity will be affected.

3.1.2 Purification process

This process consists of 3 purification phases (decantation's), which use acetone, IPA and methanol. Acetone was the most efficient solvent in separating the nanowires from the nanoparticles during the first purification phase. Other solvents were tested in this first step, but with IPA, the solution didn't show any visible separation, with ethanol, a small visible separation was observed. Both the acetone and methanol were able to separate the nanostructures successfully, however, with the acetone being more aggressive towards the solution and its inability to dissolve the PVP surrounding the nanowires, it created a big difference in weight between the two nanostructures, making the NWs precipitate and the NPs to rise. This resulted in the full decantation of the solution in about 45-60 min, with better results than methanol, which took around 24h. Also, if the proportion between the methanol and the rest of the solution wasn't correct, the decantation could take

considerably more time. Figure 3.3 shows the appearance of the AgNWs solution after the acetone decantation conclusion, with three different examples regarding the state of the solution itself.

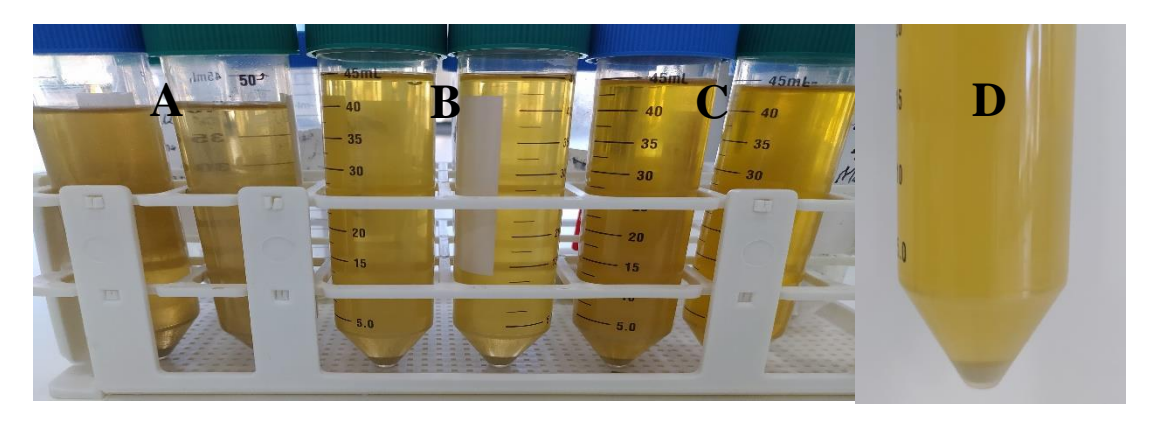


Figure 3.3 – The (A) pair of solutions was decanted with 30 ml of acetone and the (B) pair by 35 ml. The (C) pair of solutions which were oxidised was decanted by 35 ml of acetone. Image (D) shows a close up of the two phases formed after the decantation process is complete.

Three different decanted solutions were created and duplicated to test and verify the importance of the amount of acetone used, but also to see if the grey precipitate that forms at the bottom of the tube, indicates the presence of AgNWs. Although the amount of acetone poured should be at least 3 times greater than the AgNWs solution (30 ml to 10 ml), any more, doesn't affect the decantation quality or its speed. This is verified by obtaining the same results in both solutions (A) and (B) around the same time. The oxidised solution (C) was decanted, purified and observed by SEM. The results showed, the presence of AgCl and AgNPs, which verified that the grey precipitate is formed merely by high concentrations of silver and doesn't necessarly mean the presence of AgNWs. Figure 3.4 bellow shows the AgNWs appearance after each decantation.

After the acetone decantation, a great amount of AgNPs, AgCl and PVP still remained in the solution. To solve this problem a second decantation with methanol was performed, which yielded the best results. However, due to the AgNWs small size and size difference compared to the AgNPs, it took a considerable amount of time to separate them by normal decantion, with a significant quantity of AgNPs still present in the final solution and some small AgNWs still stayed in the supernatant, and were removed in the process. In order to avoid this, the decantion was made with 15 ml of methanol, placed in an ultrasonic bath to disaggregate the nanostructures, followed by a centrifugation at 2000 rpm for 30 minutes. For the third and final decantation, 10 ml of IPA and 20 ml of acetone were used along with a centrifugation at 2000 rpm for 30 min, to help clean the remaining impurities and disaggregate the NPs from the NWs. No more decantations were done, since although the solution would get purer, the number of NWs removed would also increase. The final AgNWs obtained after the supernatant removal, were diluted in 5 ml of IPA and were then ready to be characterized.

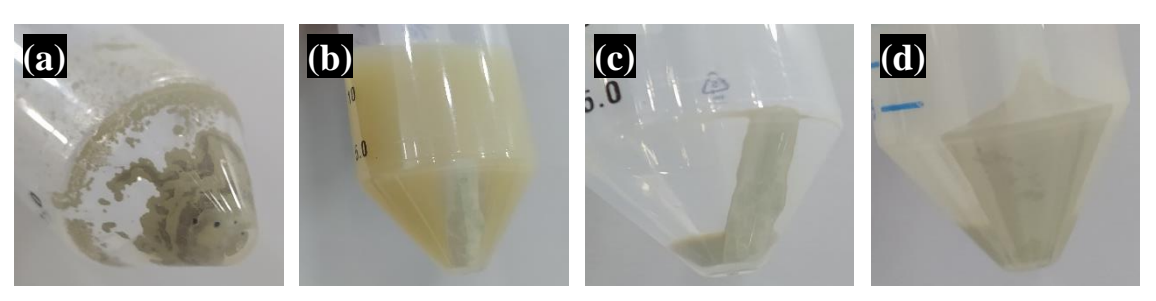


Figure 3.4 – (a) AgNWs remaining after the acetone decantation; (b) phase separation of the AgNWs (silver stream) from the supernatant (yellow solution) during the methanol decantation; (c) AgNWs remaining after the methanol decantation and the supernatant removal; (d) AgNWs remaining after the final decantation of acetone and IPA.

Most AgNPs and impurities are removed after the final purification, however, it proved impossible to eliminate them completely, resulting in their presence around the AgNWs when used in the sensor production. It is important to note that, although the microwave-assisted polyol method enables a very fast synthesis process, it was observed that even when the entirety of the process was perfectly reproduced, the solution quality still varied. This was most noticeable in the SS and an example of this can be seen in Figure 3.5 bellow.

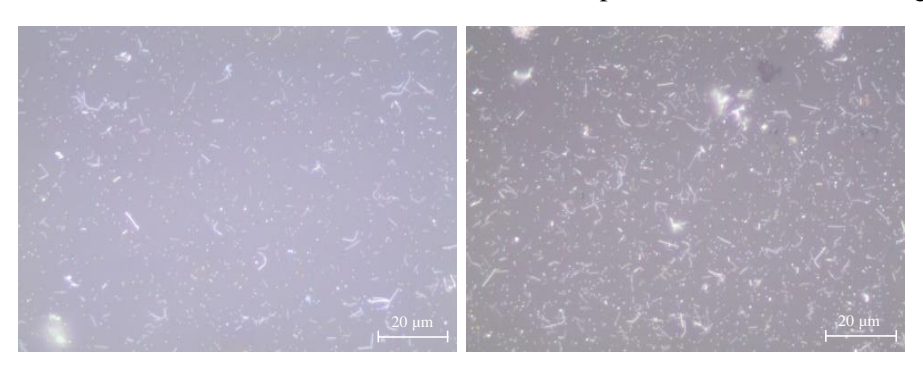


Figure 3.5 – Comparison between two optical microscope images of solutions synthesized through the SS, with the same purification process, but with different results.

Althogh perfectly reproduced, the right SS solution clearly shows a superior quality to the other. This is due to the sensitivity of the chemical parameters during the polyol process and the verified AgNWs synthesis replication failure on the microwave. The OS showed some changes, but the AgNWs quality remained almost the same, displaying a superior stability. The OS and commercial AgNWs quality are compared in Figure 3.6.

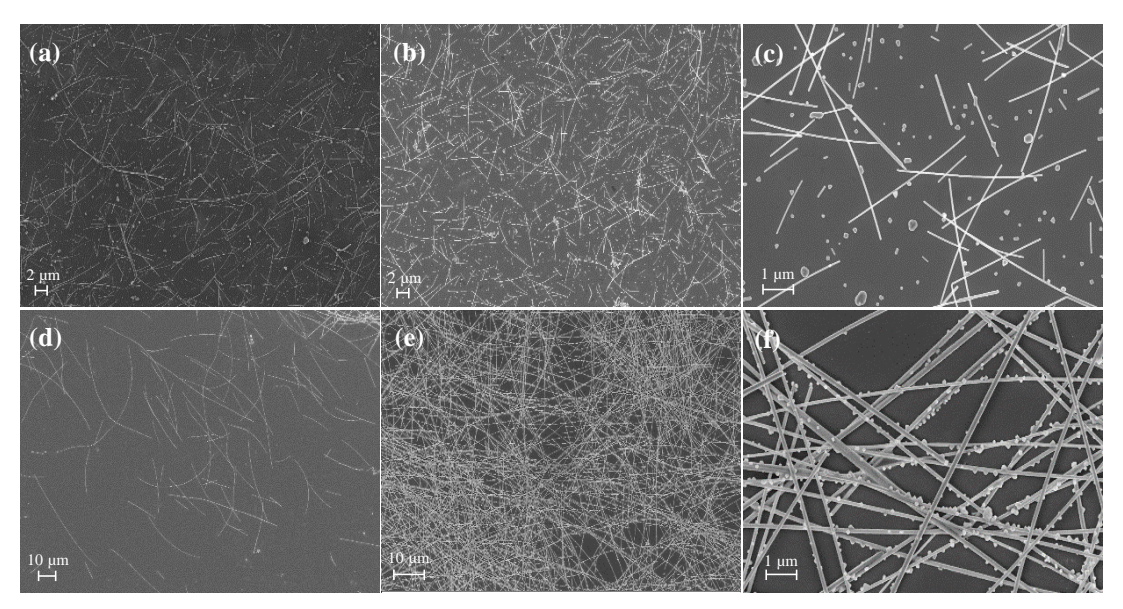


Figure 3.6 – SEM images comparing the commercial AgNWs with the ones produced using the OS. (a) AgNWs after the first purification (acetone decantation); (b) AgNWs after the final purification (acetone and IPA decantation); (c) the presence of other by-products even after the final purification; (d-f) commercial AgNWs with different magnifications.

From two OS solutions images of Figure 6.12 in the Annexes, 76 and 80 AgNWs were measured with the ImageJ software and they had a length of 1-11 μ m (with an average value of 6.42 \pm 2.20 μ m and 6.38 \pm 1.54 μ m) and a diameter of 45-80 nm. The commercial AgNWs had a length of 31.25-72.05 μ m, with a diameter of 94-265 nm. The SEM images above show a clear difference in the AgNWs sizes of the OS and commercial solutions and the amount of impurities present. The OS images above showed that the number and size of the AgNWs managed to remain almost the same from the first purification phase to the last, which means that the

number of purifications was enough to achieve a reasonable clean solution, while preserving the AgNWs. The concentration values of the SS and OS AgNWs dispersed in 10 ml of IPA were 0.58 mg/ml and 0.75 mg/ml, respectively, while the commercial AgNWs solution was 0.78 g/ml. The commercial and SS concentrations were already determined in previous works. The OS concentration value was determined with equation (3.1).

$$C = \frac{m}{V}$$
 equation (3.1)

Where, C (mg/ml) is the solution concentration, m (mg) is the mass of the solute dissolved, and V (ml) is the total volume of the solution.

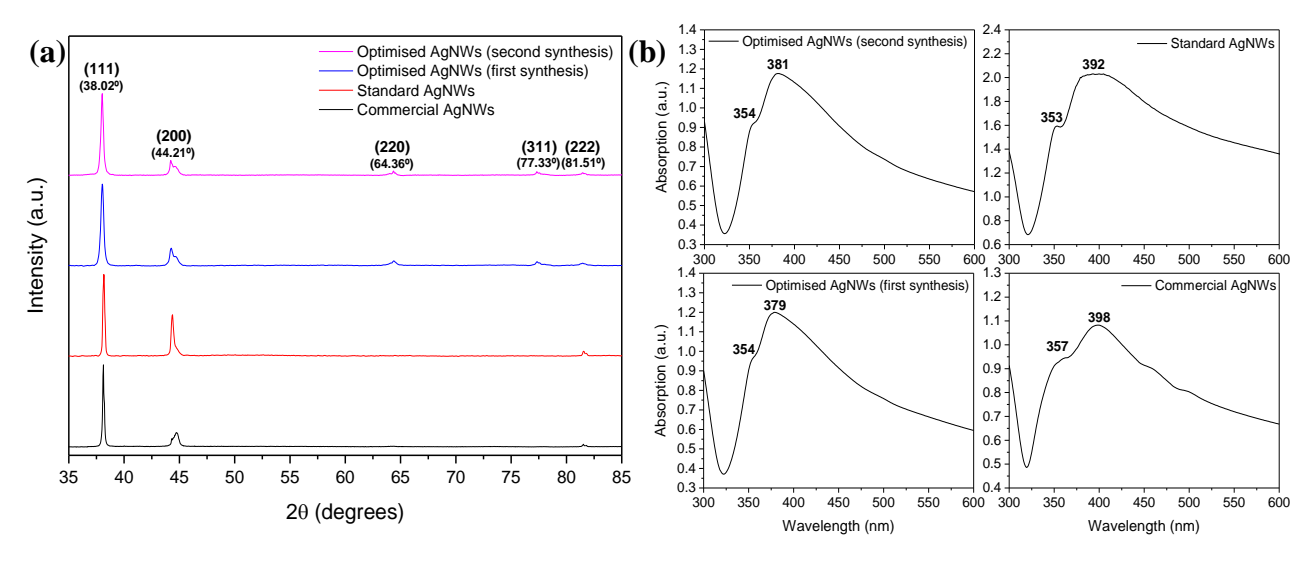


Figure 3.7 – (a) XRD analysis results of 4 different samples. (b) UV-Vis absorption spectrum analysis of 4 different samples with their respective peaks and shoulders.

The XRD analysis (see Figure 3.7- a) was done on the OS and the SS samples in order to study the crystalline structure of both AgNWs and compare them with the XRD results of the commercial sample, which exhibits a superior quality. The peaks present in the OS solution are centered at 38.02°, 44.21°, 64.36°, 77.33° and 81.51° which corresponds to the (111), (200), (220), (311) and (222) crystallographic planes of the face center cubic (FCC) of Ag [37]. However, both the SS and the commercial solution don't possess the two peaks at 64.36° (220) and 77.33° (311). This may be due to the excess of PVP present in the nanowires, or the solution was too diluted. The diffraction intensity ratios of the (111)/(200) planes for all four solutions are 5.78 for commercial, 1.98 for SS, 4.72 (first synthesis) and 5.48 (second synthesis) for the OS. Furthermore, the OS (111)/(220) planes ratios values are 17.57 and 19.61. These results showed that there was a preferential growth in the (111) plane and that the OS values were very close to the commercials ones and other AgNWs with good quality, found in literature [38]. The crystallite sizes: commercial - 43.93 nm, OS - 17.08 and 26.60 nm.

The UV-Vis absorption spectrum of the OS solutions (see Figure 3.7-(b)) exhibits one peak at 380 nm with a shoulder at 354 nm. This is due to the increase in symmetry of the AgNWs, which tends to occur when the diameter increases, the smallest peak starts to disappear and merge with the larger one, forming a shoulder instead of a peak. The SS solution has two peaks at 392 nm and 353 nm and the commercial solution has two peaks at 398 nm and 357 nm. In this last solution, the two peaks have red shifted and broaden due to the increase in the AgNWs diameter when compared to the other solutions (it's also important to note that the commercial AgNWs were heavily diluted during their analysis). All the results are in agreement with literature and to conclude, the highest peak present in all the AgNWs solutions spectrums corresponds to the transverse plasmon resonance and the other to the quadrupole resonance excitation [39].

3.2 Production of the BNC membranes

In order to create a flexible and biodegradable membrane, with the necessary mechanical properties and morphology, to be used as a substrate and as an encapsulating layer of the sensor, cubes of *nata de coco* were previously clean in order to remove all the sugar present and were then placed in a manual press (HeatPressUK, Swing-a-way) for 15 min at the maximum pressure, while sandwiched between one layer of aluminium foil and 2 layers of paper on each side. Figure 3.8 bellow, shows the BNC membrane production process.

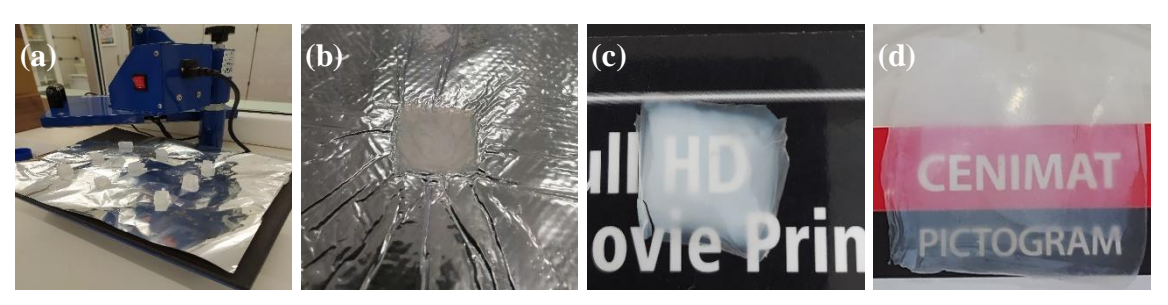


Figure 3.8 – (a) Manual press of the nata de coco cubes; (b) the resulting wet membrane after the manual press; (c) membrane after drying in a vacuum desiccator; (d) membrane after the hydraulic press.

The membranes were quickly pulled with a tweezer from the aluminium foil before they started to dry and were placed in a vacuum desiccator for 24 h at 30 °C and -55 cmHg. The resulting membranes were thin, with reasonable transparency but didn't have a uniform thickness. So, the membranes were pressed again, but with 10 tons, for 5 min, in a hydraulic press, making them thinner, with a higher transparency and a more uniform thickness. It's important to mention that the only two characteristics needed for this sensor to have a good performance are a smooth surface and a uniform thickness, a high transparency is not necessary. Moreover, it was later discovered that the freeze-drying process yields better results when compared to the others in regards to thickness, smoothness and the membrane mechanical properties.

A tensile test was done in order to attain a stress-strain (σ - ε) curve, to know the ultimate tensile strength (UTS), the fracture and Young's modulus (E) values of the *nata de coco* membrane. Two tests were performed, the first was done to a simple dried nata de coco membrane and the second to 2 membranes glued together in the middle by a thin line of solvent free glue, to observe how the membranes would react to the glue before being used to encapsulate the sensor. The results of these tests are displayed on Figure 3.9.

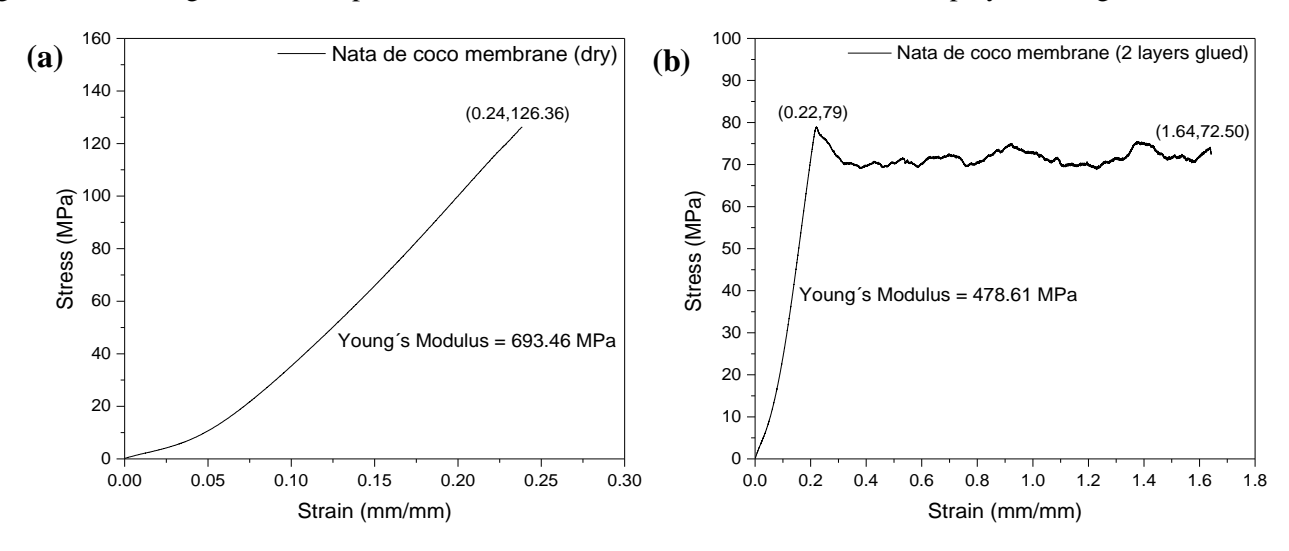


Figure 3.9 – Stress-Strain $(\sigma$ - $\varepsilon)$ plots of the dry *nata de coco* membrane (a) and the two membranes glued together (b).

The dry membrane sample had 3.4 mm of width (W), 26.5 μ m of thickness (t) and was held tight by two claws with 1.25 mm distance between them (L_0). The data came in the form of load (N), which is the traction force applied to the sample (F), and stroke (mm), which is how much the sample stretched (ΔL). So, in order to obtain the respective stress-strain (σ - ε) curve, the equations (3.2) and (3.3) were used [40].

$$\sigma = F/(t \times W)$$
 equation (3.2)

$$\varepsilon = \Delta L/L_0$$
 equation (3.3)

The resulting stress values are in MPa and the strain is dimensionless. The left stress-strain curve plot in Figure 3.9, shows that the membrane has a brittle structure, indicated by the lack of plastic deformation with no change to the strain rate before its fracture. Also, due to the lack of plastic deformation the UTS and fracture have the same value of 126.36 MPa which is comparable with other tensile tests done to *nata de coco* found in literature [40]. The membrane also has a very low deformation value, only stretching 0.298 mm, which corresponds to 0.24 strain or a 24% increase in length from its original size. This is due to the drying process and to the 10-ton pressing done on the membrane which extracts most its moisture leaving the fibers very dry, limiting their stretching and mobility to change from their random orientation and align with the force direction. However, for the performance of the sensor, this is a very good characteristic to have, because, if the sensor happens to be placed under high amounts of stress, the results show that, the resulting deformation of the substrate and consequently of the interdigitated electrodes, printed on its surface, are kept to a minimum and therefore will not influence the sensor performance. Furthermore, the Young modulus of this sample is 693.46 MPa, which is higher than the reported literature [40], due to the low strain value of the sample.

The sample used on the second tensile test consisted of 2 membranes glued together in the middle section, by a thin line of glue, with 1 mm width and a length equal to the sample. The membranes had a 3.0 mm width and a joint thickness of 55 µm. By analysing the results, a very different behaviour can be observed when compared to the dry sample, which is consistent with a ductile material with plastic deformation. This sample has a UTS and a yield strength of 79 MPa with a corresponding 22.07 % strain, a fracture value of 72.50 MPa, with a total deformation of 2.05 mm (164.2% strain) and an expected lower 478.61 MPa Young's modulus, which is still within the standard value for the *nata de coco*. The different behaviour of this sample was due to the applied glue, because the cellulose polymer being a polar compound with great affinity to itself and materials containing hydroxyls, especially water, combining it with the excellent water holding capacity (WHC) and moisture retention capacity (MRC) of the BC [41][42], it created good conditions for the area on the BNC in contact with the glue to become more hydrated by draining most of its moisture, preserving it between the two membranes and retaining it by far more time than expected.

The glue in this situation ended up acting more like a lubricant, which resulted in the test being performed while parts of the membranes were still wet. So, in the elastic regime, the two membranes glued together, behaved exactly like the dry membrane, until reaching a stress value of 79 MPa, which with the help of the glue acting as a lubricant and giving the fibers the necessary mobility, was enough pressure to align some of the fibers, enabling them to stretch by far more than the ones in the dry membrane. The erratic behaviour of the constant increase and decrease in the stress values displayed in the plastic region was due to machine noise and the increasing number of align fibers until the membrane fracture.

The behaviour of the last discussed sample could have been avoided by using an oil-based glue, which is non-polar and therefore won't be absorbed by the membrane. When used in small quantities, the used glue has a shorter drying time, however, after some time the membranes separate completely. Using a larger amount of glue ensures this does not happen, but it takes more than 1 day to dry at room temperature. Drying in a rapid way, using high temperatures, makes the membrane start to wrinkle, which would prove difficult to be used

during encapsulation, since a small pressure must be applied while it dries and the membrane in contact with the tissue paper must be stable. Figure 3.10 shows the BNC wrinkles, bacteria and its random network pattern.

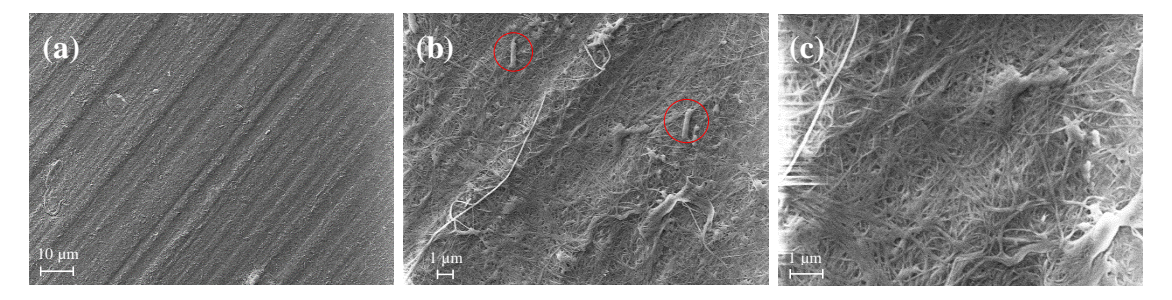


Figure 3.10 – (a) SEM images of a dry membrane wrinkles produced when it shrunk during the drying process; (b) the Acetobacter xylinum bacteria (red circle); (c) the BNC fibers appearance with their random network pattern.

The dry membrane on the macroscopic scale appears to be perfectly smooth, however by analysing it on SEM, a very small ripple effect (wrinkles), can be observed in the membrane structure. The wrinkles shown, are the result of the membrane shrinking during the drying process, but later successufully minimised during the hydraulic press phase. The individual fibers can be seen on Figure 3.10-(c) and when analysed, their fiber network displays a random pattern, which helps support the results for their similar mechanical strength to traction in all directions. It's also possible to observe the different length and diameter of each fiber. The wrinkles, pores and fibers diameters were measured using the ImageJ software and are displayed in the Table 3.1. Some cylindrical shape organisms highlighted with a red circle (see Figure 3.10-(b)) can be seen on top of the fiber network, these are the left over Acetobacter xylinum bacteria that produced the BNC fibers and managed to remain on the membrane until this point. They can also be observed in various papers [43][44].

Table 3.1 – Diameter of some of the wrinkles, pores and fibers present in the nata de coco membrane.

| Sample diameter | | | | | | | | |
|-----------------|-----|-----|----|-----|-----|-----|-------------|--|
| Fiber (nm) | 59 | 44 | 56 | 50 | 52 | 58 | 53.17±5.67 | |
| Pore (nm) | 57 | 35 | 46 | 68 | 40 | 65 | 51.83±13.56 | |
| Wrinkle (µm) | 0.9 | 1.2 | 2 | 2.5 | 2.9 | 4.0 | 2.25±1.14 | |

The fibers diameters and the pores sizes obtained in this work are in agreement with other BC in literature [45][46]. However, due to the heavy pressing of the nata de coco to turn it into a very thin membrane, the fibers diameters are larger and the pores smaller than their original size. The BNC membrane XRD, FTIR and AFM results displayed a high purity and low roughness (Annexes-Figure 6.5, Figure 6.6 and Figure 6.7).

3.3 Screen printing of the interdigitated electrodes

The interdigitated electrodes were produced on the *nata de coco* membrane surface to serve as a fast conduit of the applied voltage that uses the sensing material as a bridge to connect both sides. A CRSN2442 nanoparticle conductive silver ink was used, because of its excellent conductivity, good permeation on the membrane and facile deposition with screen printing (due to its viscosity and excellent results with a minimal annealing time of 5-10 min at 105 °C). The screen-printing method was used due to being low cost, very compatible with cellulose, fast and easy to do. Figure 3.11 shows the IDEs produced on the membrane surface.



Figure 3.11 – Materials and method used to fabricate the IDEs on the membrane surface and the resulting product.

The IDEs were printed on PET and BNC, to compare the BNC membrane with a widely used substrate. AFM (Figure 6.7 in the Annexes) and SEM analysis were performed on the interdigitated electrodes to observe how its morphology would change when printed on different surfaces. The results are shown on Figure 3.12.

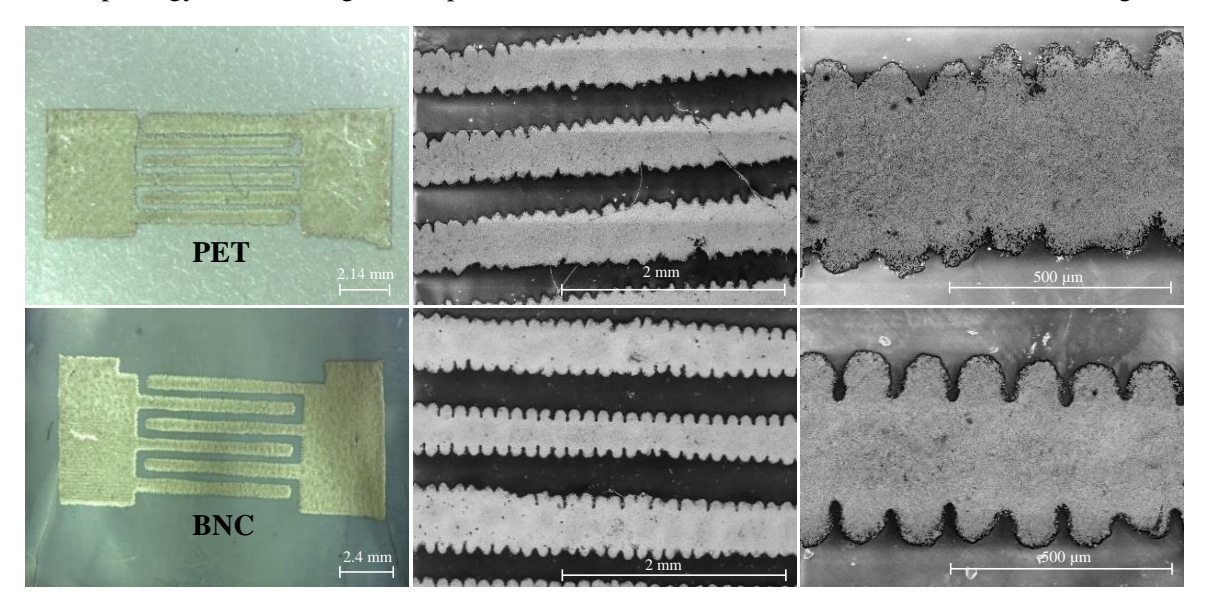


Figure 3.12 – Optical stereo microscope and SEM images of the IDEs and their respective finger electrodes printed on both BNC and PET substrates.

The PET (first row) and BNC (second row) images in Figure 3.12 were obtain by a Optical stereo microscope Leica M80 and by SEM. In the optical microscope images, a more define printing pattern can be seen on the BNC, with an overall better resolution and resistance to damage by the multimeter tips. The images on the second and third collumn show a reacuring pattern on the finger electrodes of both substrates, composed of small circles and being more define in the BNC. Also, its possible to observe that the BNC has more finger electrodes with different sizes, due to the ink permeation on the membrane, caused by its superior absorption capacity and porosity, which causes the spreading of the ink to vary more before drying. The measurements of the BNC conductive finger eletroctrodes dimensions were made with the ImageJ software and presented an average width of 0.51 mm, a length of 7.14 mm and a distance between each finger electrode of 0.26 mm.

A folding test was applied to both substrates to see how the resistance values of the finger electrodes would vary when submitted to various foldings cycles, but also to enable a direct comparison of the stability and flexibility of both substrates. They were then submitted to 250 inward (+180°) and 250 outward (-180°) folding cycles. After the folding test, they were folded inward to have a better view of their interdigitated electrodes and were placed side by side on a glass surface. Figure 3.13 shows the structural state of both substrates after a fast initial structural recovery (left image) and after 24 hours (right image).

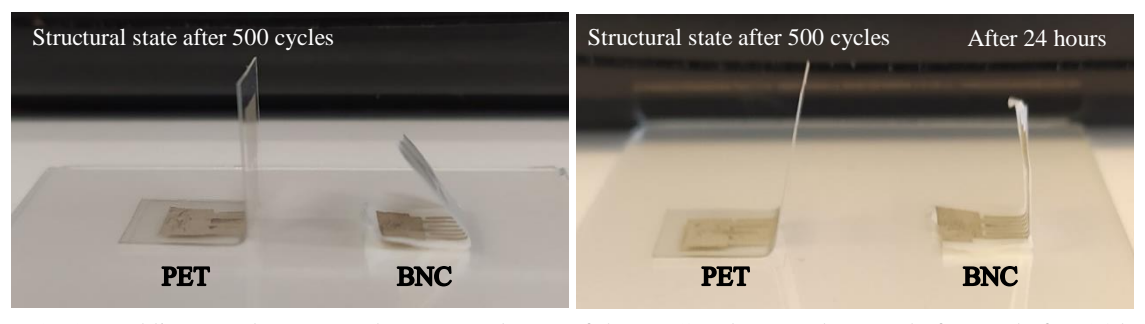


Figure 3.13 – Folding test damage on the structural state of the BNC and PET substrates before and after 24 hours.

Immediately after the test, PET recovered most of its initial form, while the BNC did not. This is due to their difference in flexibility and as mentioned before, the BNC membrane is very thin and possesses no elasticity to traction due to its very dry fibers. However it can be crumpled and put back together with ease, can be folded as many times as possible by the amount of force applied and has excellent flexibility. These characteristics are shared with all celullose based materials to a certain extent. Its possible to see that, after 24 hours the BCN recovered almost double of what it did before, while PET showed little change.

Table 3.2 – BNC and PET electrical resistances throughout the folding test.

| Folding Cycles | 0 | 50 | 100 | 150 | 200 | 250 | 300 | 350 | 400 | 450 | 500 |
|-----------------------|-----|----|-----|-----|-----|-----|-----|-----|-----|-----|-----|
| BNC (Ω) | 0.5 | 1 | 1.3 | 1.6 | 1.8 | 2.1 | 2.5 | 2.6 | 2.9 | 3.0 | 3.1 |
| PET (Ω) | 1.1 | 7 | 13 | 17 | 20 | 24 | 36 | 47 | 69 | 97 | 137 |

A 1 cm² conductive silver ink square was printed on both substrates and measured with a four point probe to have an accurate measure of the ink electrical resistance. The BNC and PET values were $0.054~\Omega/\text{sq}$ and $0.079~\Omega/\text{sq}$, respectively. However, due to the small finger electrodes sizes, their electrical resistances had to be measured with a multimeter during the folding test. The two tips were place at the extremities of the finger and the resistance was measured in the same place with the same tip interval distance. During the folding test 500 cycles were performed in total to both substrates and altought they started with similar initial resistances, it is possible to see on Table 3.2 that the PET resistance increased much more during the first 250 cycles (+180°) when compared to the BNC that had almost no change. In the last 250 cycles (-180°) which causes the most damage, the electrical resistance on PET increased dramatically, while the BNC maintained an linear increase. Also, due to the very low mechanical resistance of the BNC to folding (it folded very easily), a greater pressure had to be applied for an increase in electrical resistance to take place, when compared to PET.

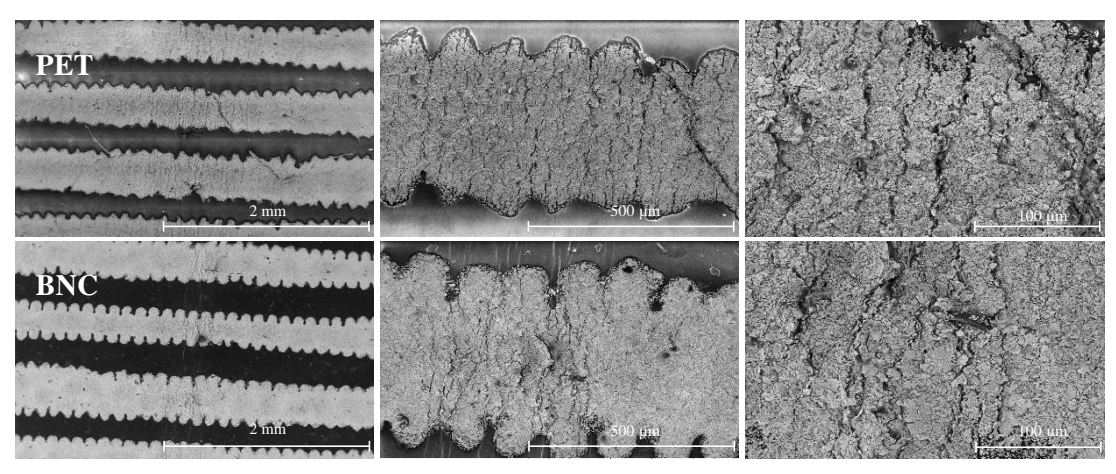


Figure 3.14 - SEM images of the finger electrodes appearance on both PET and BNC substrates after the folding test.

After the folding test, fractures and peeling of the ink appeared on both substrates (Figure 3.14), which were more severe on the BNC, due to the extra pressure applied. Nevertheless it showed better results, due to the permeation of the ink on the membrane, allowing it not only to conduct on the surface, but also beneath it through the fibers, which helped maintained its original electrical resistance value more successfully than PET.

3.4 Coating of the tissue paper with AgNWs

The AgNWs coating of the tissue paper was achieved with two different methods, spray and dip coating. The OS was only achieved during the experimentation of the dip coating method and while it succeeded in coating the tissue paper with a network of AgNWs by using both methods, the SS solution didn't, needing some extra steps to do it. Nonetheless, the deposition of the AgNWs on the paper was successfully optimized for spray and dip coating on both syntheses. The paper types used for coating are on the Annexes - Table 6.4.

3.4.1 Spray coating

The first method tested was the spray coating and the paper used was Whatman grade 2. The paper was placed on a hot plate covered by aluminium foil at 90-100 °C, secured with Kapton tape. The SS solution was diluted in IPA and placed inside a vial connected to the airbrush. The N₂ pressure was adjusted and a fixed height for deposition established (1 bar and 5 cm). Figure 3.15 shows the spray coating process.

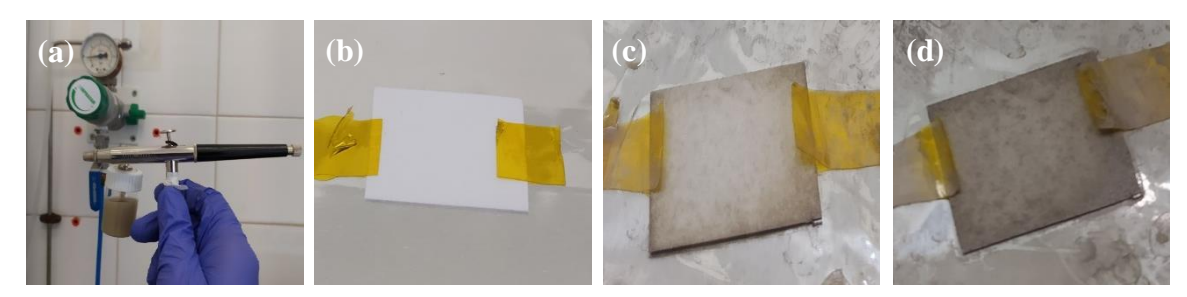


Figure 3.15 – 5 ml of AgNWs diluted in 10 ml of IPA (a) airbrush XL2000, (b) no solution sprayed, (c) half flask (7.5 ml sprayed), (d) full flask (15 ml sprayed).

The coffee ring effect was the first problem to appear and was caused by excessive N_2 pressure and insufficient height (1 bar and 5 cm), which resulted in more AgNWs to be deposited away from the center. The paper became very quickly saturated due to the high flow of solution and the lack of time for the solvent (IPA) to evaporate. This could not be corrected with more quantity or different solution concentrations and presented a critical problem for the overall electrical resistance of the paper. So, an optimisation of pressure and height during deposition was required. The results after the optimisation can be seen on Figure 3.16

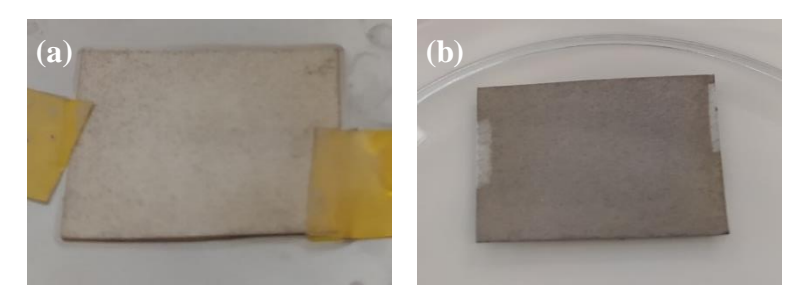


Figure 3.16 – 15 ml sprayed. (a) 1 ml of AgNWs diluted in 14 ml of IPA, (b) 3 ml of AgNWs diluted in 12 ml of IPA.

The coffee ring effect was successfully minimised by changing the height and pressure to 10 cm and 0.5 bar, however, the lower pressure and increased height also resulted in the deposition process becoming more difficult to control and lasting longer. The solution concentration was also changed to demonstrate that despite a lower concentration, better results could be achieved with a more correct deposition process. However, despite many attempts only one solution of the SS had enough quality to coat the paper with the AgNWs and make it conductive enough to be used, its results can be seen on Figure 3.17. The paper achieved an electrical conduction of 743-1382 Ω /sq in the center and 88-399 Ω /sq in the perimeter with 3 ml, but it also coated many nanoparticles and PVP remains. This turned the process of achieving a desired electrical resistance very difficult and since the solution could not be reproduced, this experimentation and its results served only as an example, to show that, with a proper solution and deposition process, the paper can be made conductive.

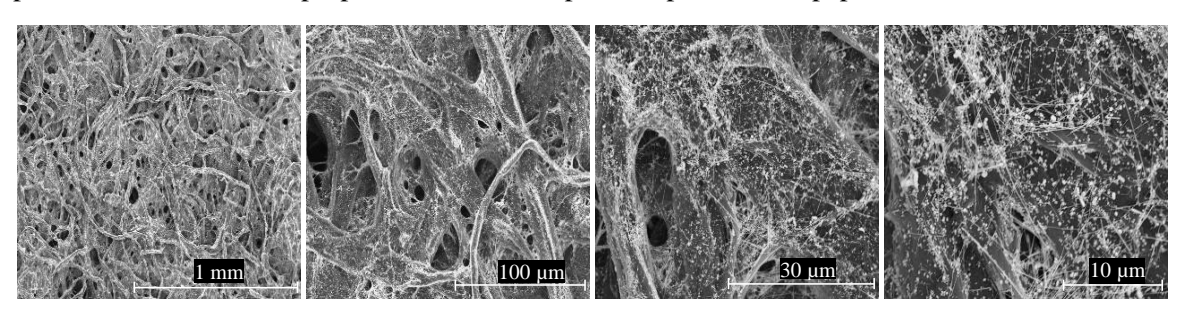


Figure 3.17 – SEM images in different magnifications of the Paper Whatman grade 2 spray coated with 3 ml of the conductive SS solution diluted in 12 ml of IPA.

The OS solution was able to make the paper Whatman conduct with only 1-1.5 ml, but the different resistance values across the paper persisted and it was still a time-consuming process. This could be corrected by using a spray coating unit, which achieves better and more stable results, since the problems originate by lack of control and human error. However, it will still take considerable time to coat the paper. Laser welding was applied on the paper to correct some of the problems and decrease the amount of solution used, but wasn't successful (see Annexes Figures 6.1-6.2). So, the spray coating method wasn't used in the sensor production.

3.4.2 Dip coating

Kimberly and Tork papers, were chosen for the dip coating process, since they displayed better results than the other two tested papers (Whatman and Korean paper) in preliminary tests. They were easier and faster to coat, and had a more uniform electrical resistance, which is mainly due to their smaller thickness. For this method the paper chosen is just submerged in an AgNWs solution and then dried on top of a hot plate. This is repeated multiple times to achieve a desired electrical resistance with less value variation across the paper.



Figure 3.18 – The dip coating process on the paper Tork and its appearance with the AgNWs before and after annealing.

Figure 3.18 above shows the dip coating process done on a paper Tork. The paper stays completely submerged and still for 30 seconds to soak the solution and let the AgNWs bond to the fibers. Then, the paper

is slowly pulled to let the unabsorbed solution fall to better control the gained electrical resistance in each cycle, then its placed on the hot plate for 5 min at a temperature between 90-100 °C to evaporate the solvent and unify the nanowires to the fibers. After the paper is completely dried, the electrical resistance is measured with a multimeter and if its value is adequate, the electrical resistance is then measured more accurately with a 4-point probe. This process is repeated until a desired electrical resistance is achieved. Usually 1-1.5 ml of solution is enough to dip coat the paper 4 to 10 times. The results of this process can be seen on Figure 3.19.

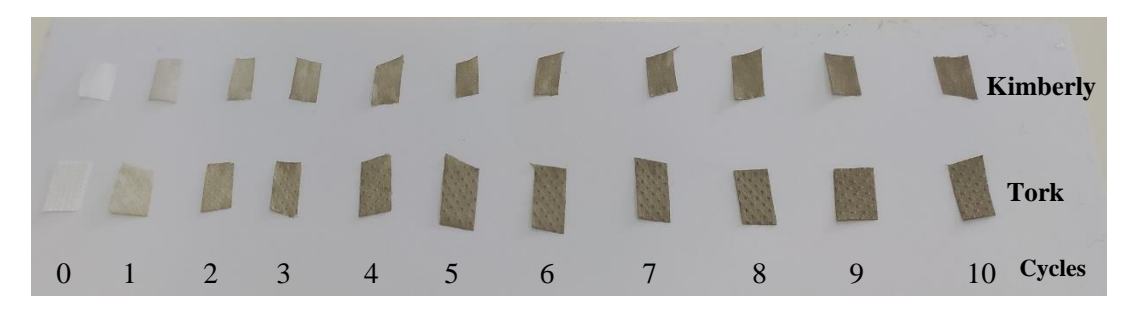


Figure 3.19 - Physical appearance of both Kimberly and Tork papers (already dry) throughout 10 dip coating cycles.

Kimberly and Tork papers were dip coated 0 to 10 times (cycles) and by analysing the results, it was possible to see that, after 3 cycles the Kimberly paper was fully covered with AgNWs, with very small empty spaces. Paper Tork achieved full coverage around 4-5 cycles, however, the Kimberly paper coverage changed with each sample, maintaining very small zones with low AgNWs density until 10 cycles. Once high concentrated areas of AgNWs start to form, they will attract even more nanowires, leading to the creation of high and low density areas. This effect can be observed in the SEM images of Figure 3.20. The 5 cycles on the Kimberly paper is an exception and may be due to a slight variation on the dip coating process during the sample preparation. Sample resistivity (ρ) , resistance (R), sheet resistance (R_5) , length (L), width (W), thickness (t), current applied (I) and voltage recorded (V).

$$R_S = \frac{\rho}{t} = 4.532 \frac{V}{I}$$
 equation (3.4)

$$R = R_S \frac{L}{W}$$
 equation (3.5)

The paper Tork voltage was measured with a 4-point probe, by applying a small current and its sheet resistance was determined with the equation (3.4) [47]. The Kimberly paper could only be measured with the use of a multimeter (the 4-point probe couldn't detect any values) and its respective sheet resistance was determined by using equation (3.5) [47]. Kimberly and Tork papers had a respective thickness of 65µm and 90µm. It was not possible to measure the electrical resistance for samples with less than 6 cycles, due to the lower number of AgNWs present and the porosity of the paper itself. However, this does not mean they don't conduct, since the 4 and 5 cycles papers Tork were successfully used on the sensor and displayed good results.

Table 3.3 – Sheet resistance values of the 10 dip coating cycles done with the OS on both Tork and Kimberly paper.

| Dip Coating Cycles | 4 cycles | 5 cycles | 6 cycles | 7 cycles | 8 cycles | 9 cycles | 10 cycles |
|---------------------------|----------|----------|------------|------------|---------------|-------------------|-----------------|
| Paper Tork (kΩ/sq) | / | / | 26.08±7.33 | 13.19±4.35 | 2.84±1.67 | 1.28±0.77 | 0.87±0.65 |
| Paper Kimberly (kΩ/sq) | / | / | / | 9258±5996 | 4458 ± 2143 | 22.99 ± 16.95 | 6.35 ± 3.04 |

Figure 3.20 shows 0,1,2, 4,5,6,8 and 10 cycles Tork papers with the OS solution. As the number of cycles increases, so does the number of high concentrated areas, since the AgNWs tend to anchor to each other.

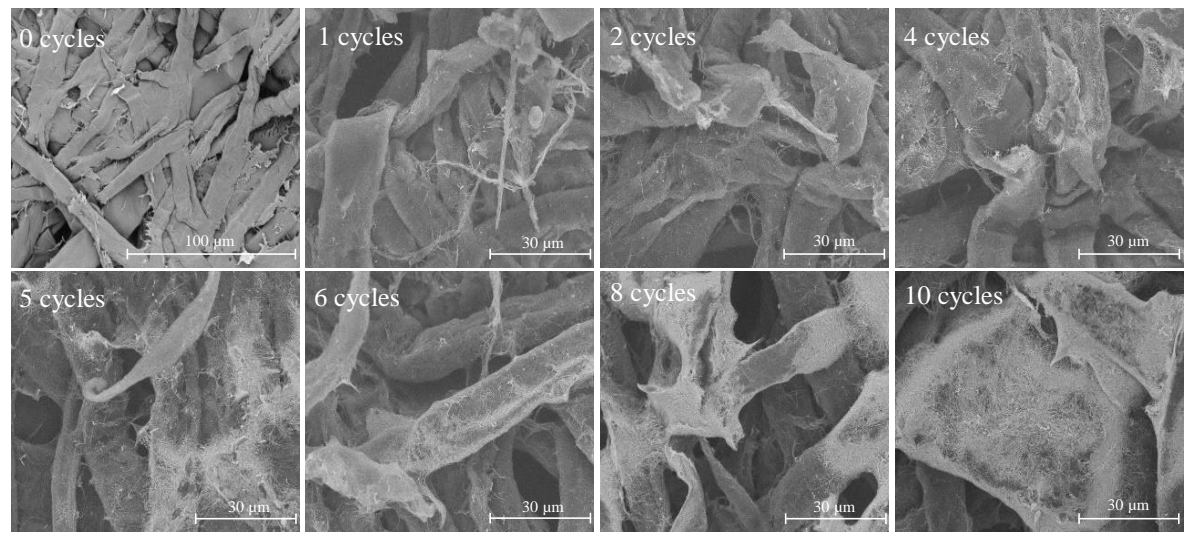


Figure 3.20 – Hitachi Tabletop SEM (with a filter that highlights the contrast between the zones with high and low AgNWs density) images of the paper Tork with 0,1,2,4,5,6,8 and 10 dip coating cycles with the OS AgNWs solution.

Although the paper appears to not be fully covered with NWs due to the filter, Figure 6.4 in the Annexes shows SEM-FIB (no filter) and Hitachi Tabletop SEM (with the filter) images of the 10 cycles Kimberly paper fully covered with the OS AgNWs, exhibiting an electrical resistance of $6.35\pm3.04~\mathrm{k}\Omega/\mathrm{sq}$. To conclude, the dip coating presented better results than the spray coating, with the paper Tork also being the best to use.

3.5 Pressure sensor performance

The AgNWs paper Tork was placed in the middle of the printed interdigitated electrodes and encapsulated with a BNC membrane (see Figure 3.21). The sensor was then submitted to 3 tests to measure its overall performance. The first test was done to see if the sensor was able to translate a specific stimulus into a current-time plot and to measure the response and recovery time of the sensor to various pressures and pressure durations, applied by a human finger. The second test was to observe if the sensor had enough stability to produce quality results for an adequate amount of time, by having a machine applying the same pressure over a certain number of times and see if the current produced remained the same. The third test served to measure the sensor sensitivity, defined as the slope of the output characteristic curve, which translates to how much output change the sensor provides between two pressures and its value was determined by using equation (1.1).

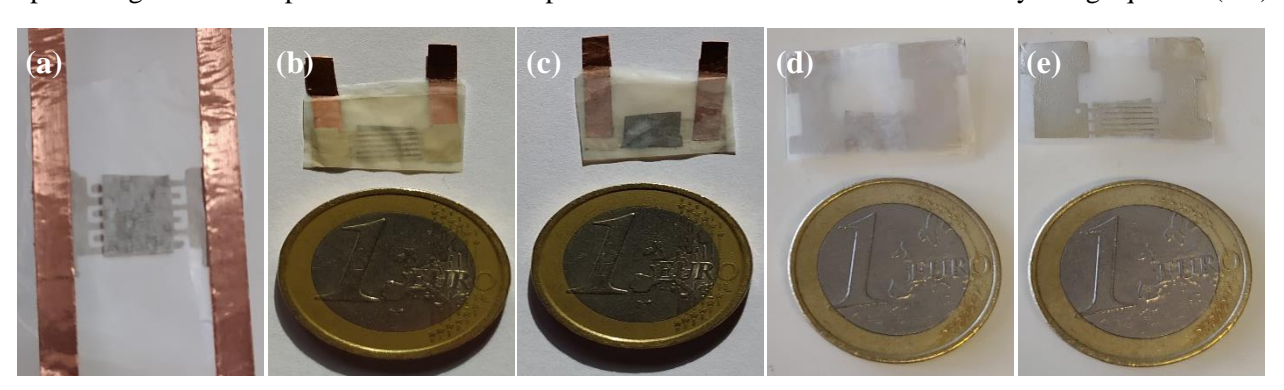


Figure 3.21 - (a) sensor not encapsulated with the BNC membrane. View of the encapsulated sensor from the front (c,d) and back (b,e). (b-c) in natural light with copper strips attached, (d-e) without copper strips in artificial white light.

All the following results are of the sensor with the Paper Tork, due to showing the best performance in preliminary tests. The 4, 5 and 6 dip coating cycles displayed the best results in preliminary tests so the different effects of these three on the sensor parameters were analysed and compared. A potentiometer was placed in series with the sensor to function as an auxiliary resistance, in order to help measure the current that passes through the sensor, to stabilise the signal and reduce the noise measured by the Tektronix TBS 1000C series digital oscilloscope. To reduce the noise during measurements even more and to have a clearer signal during low pressure measurements, 2 V were applied from a KEYSIGHT 33500B series waveform generator.

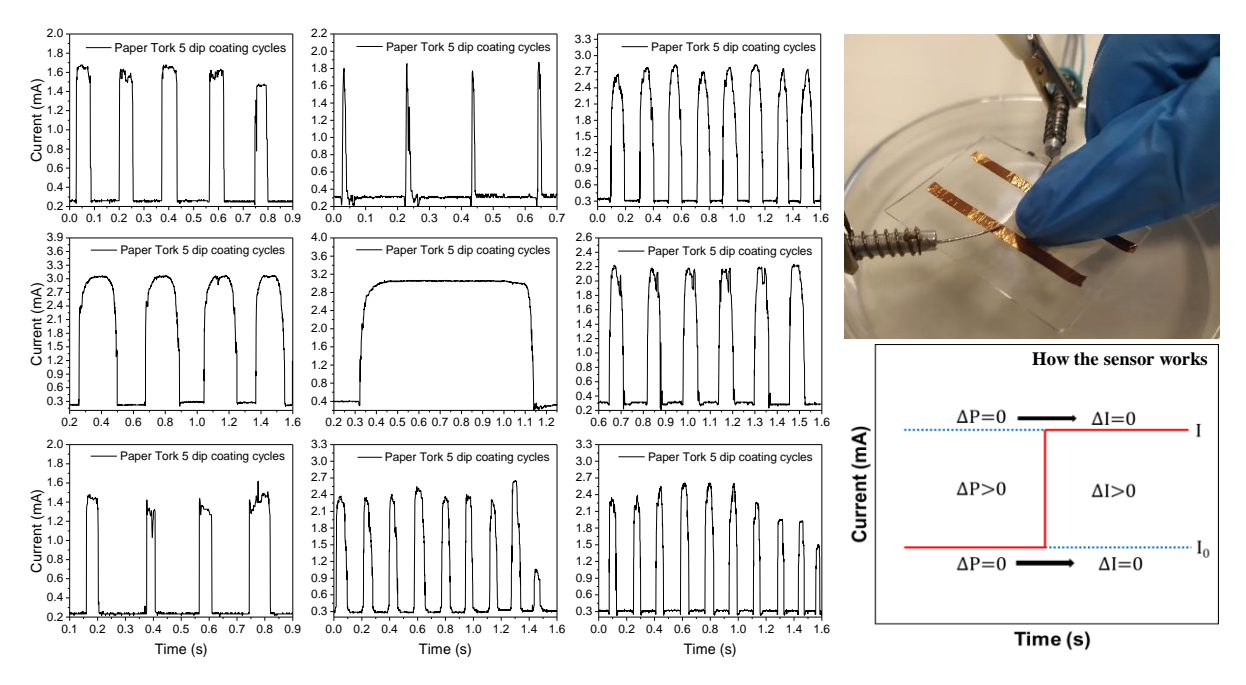


Figure 3.22 – Current-time plots of different pressures and pressure durations applied by a finger (so the pressure values couldn't be measured) to the paper Tork sensor $(0.7 \times 0.5 \text{ cm})$ with 5 dip coating cycles and the potentiometer at 571 Ω .

The test results of the 5 dip coating cycles sensor displayed on Figure 3.22, shows that it was capable of translating the different pressures and pressure durations applied by a finger (pressure can't be measured), into a current-time plot and differentiate between them (the higher the applied pressure, the higher the current).

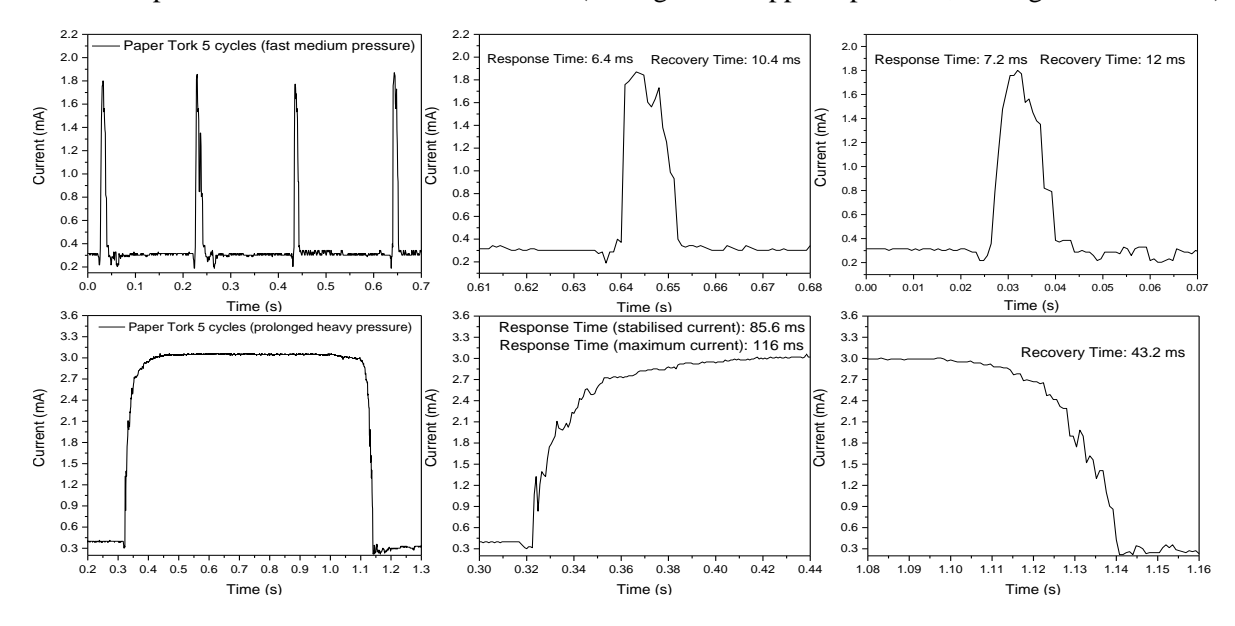


Figure 3.23 – Response and recovery times of a fast-medium pressure (images on the first row) and a prolonged heavy pressure (images on the second row) applied by a finger on the paper Tork with 5 dip coating cycles.

The results of Figure 3.23 show that the response and recovery time of the sensor with the 5 dip coating cycles paper Tork, were as low as 6.4 ms and 10.4 ms for a fast-medium pressure, which can be considered very fast when compared to other paper based sensors in literature [29] and very similar to other piezoresistive sensors with different components [35][36]. However, when a prolonged (long duration) heavy pressure was applied, the values were very different, reaching a response and recovery time of 85.6-116 ms and 43.2 ms. This was due to the slower pressing, but mainly due to the slower current rise near high pressure values, where the sensor is reaching its compression limit and has connected almost all of the available AgNWs. The sensor structure was also more damaged in this situation, which increased the recovery time significantly.

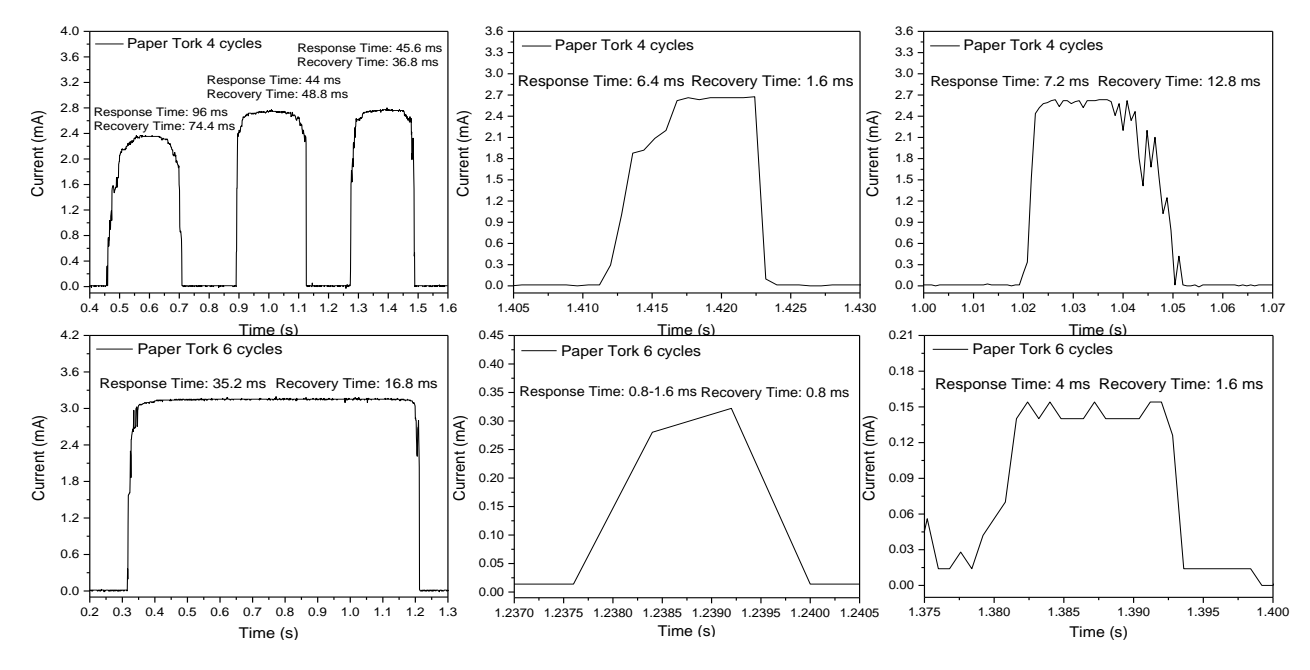


Figure 3.24 – Response and recovery times of the sensor with 4 and 6 dip coating cycles under different pressures and pressure durations applied by a finger (so the pressure values couldn't be measured) with the potentiometer at 571 Ω .

In Figure 3.24, the sensor with the 4 dip coating cycles exhibited a similar overall performance to the 5 cycles, but surpassed it in the recovery time with 1.6 ms, due to the lack of vibration and additional touch by the finger, which happened on the 5 cycles examples. However, a less conductive paper having a superior response or recovery time doesn't necessarily prove its actually faster. It's important to remember that this test was made by hand and its limited to the user speed and control, a more conductive paper will always be faster. The first objective of this test was to observe if the sensor could translate the different applied stimulus, which it did. The second objective was to obtain the response and recovery times of the sensor with the 4, 5 and 6 dip coated papers. Although, it was not possible to have a good comparison between the 4 and 5 dip coating papers. The 6 cycles paper Tork, demonstrated a superior value in both response and recovery times, exhibiting 0.8-1.6 ms and 0.8 ms respectively, due to being more conductive and therefore, the current will travel faster.

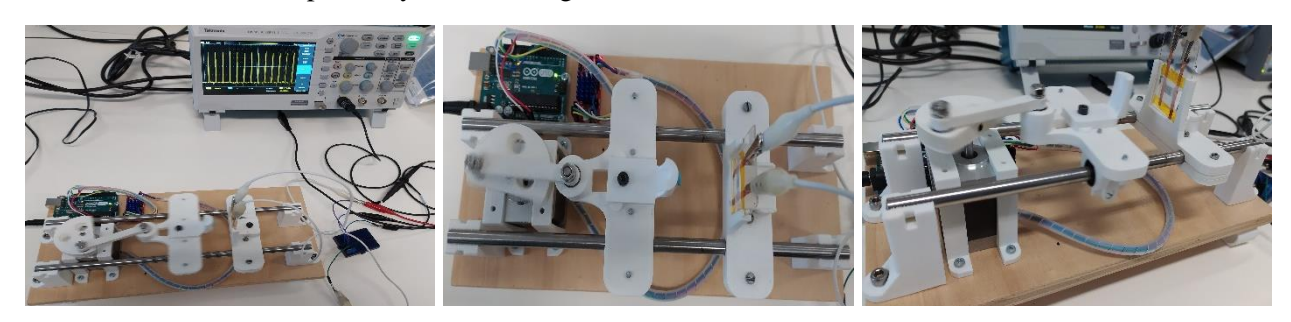


Figure 3.25 – Machine with Arduino Uno and setup used to perform the stability test to determine the sensor stability.

In order to determine the sensor stability, the sensor was taped to the center of a piece of glass with used Kapton tape, then it was placed between the two white supports seen in Figure 3.25 and by using the software Arduino, the machine was programmed to hit the middle of the sensor 15000 times at a frequency of 1 Hz.

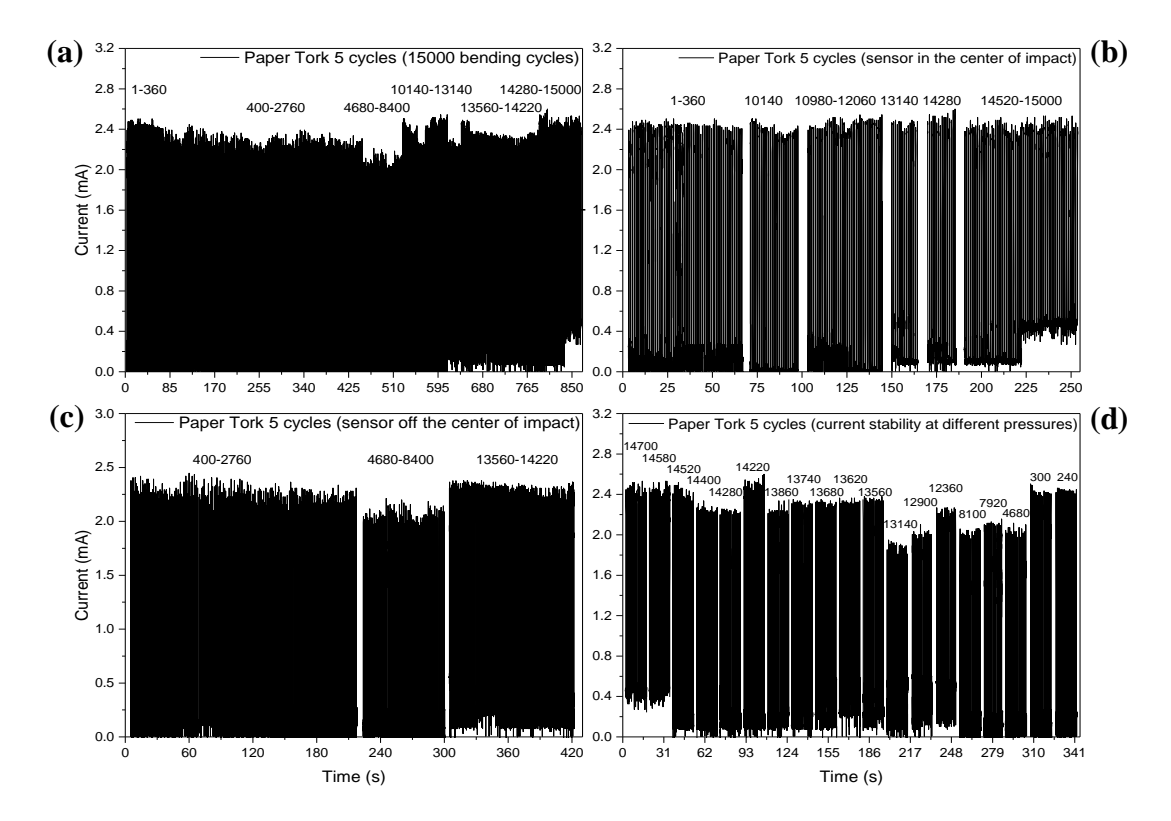


Figure 3.26 – Stability test performed on the sensor with the 5 dip coating cycles paper Tork. Image (a) shows the stability results of the full 15000 cycles test. (b) results of the sensor in its correct/initial position. (c) results of the sensor, with the pressure applied in a different location, due to a change in the sensor position, caused by the machine over a period of time. (d) results of the sensor under different pressures, at different times during the stability test.

The pressure of the impact done by the machine, could not be determined, since there weren't any means available at the time. The results were recorded with various time scales in the oscilloscope, to obtain an accurate reading of small and large samples. On Figure 3.26, the first 360 cycles showed a stable current value, however, at the 400 cycles, the current started to vary around a certain value until the 2760 cycles. At the 4680 cycles, the current value dropped by a significant number, the cause of this was the non-ideal setup used for the test, which also affected the stability of the small initial current established before the test. The machine could only be programmed to hit the target with specific speed not force and there was a small gap in thickness between the glass and the two white supports, which resulted in the glass/sensor shaking with every hit. After a certain number of hits, the glass started to change its position slightly and therefore, changing the location where the machine hits the sensor, which resulted in different applied pressures and their respective currents.

Since the current values continued to decrease, the glass/sensor was placed in its original position around the 10140 cycles. This procedure was done 2 more times, after every significant change in its position, until the 13140 cycles mark. The return to its original position is displayed by the 3 peaks in current at 528-654s, where the values are similar with the ones around 1-360 cycles. At the same time a slightly higher initial pressure was applied at 614s, this increased the initial current value and made it more stable, without returning it to 0 mA every time the machine touched the sensor. Once again, the sensor was placed in its original position at 14280 cycles and the glass was strongly held in place during the current values recording. This is showcase by the fourth and last large current rise around the 689s mark. The glass was fixed in placed at 835s and the

initial current was increased further. The current values during the 14520-15000 cycles were nearly the same as the first 360 cycles, but less stable as expected. Although the conditions during the test were not ideal, the objective to show that the sensor displays high stability at the end of 15000 cycles was achieved. Furthermore, by analysing small and large samples of currents in Figure 3.26-(b-d), it shows that, even with different applied pressures, they all displayed high stability. However, the results got worse as the number of cycles increased.

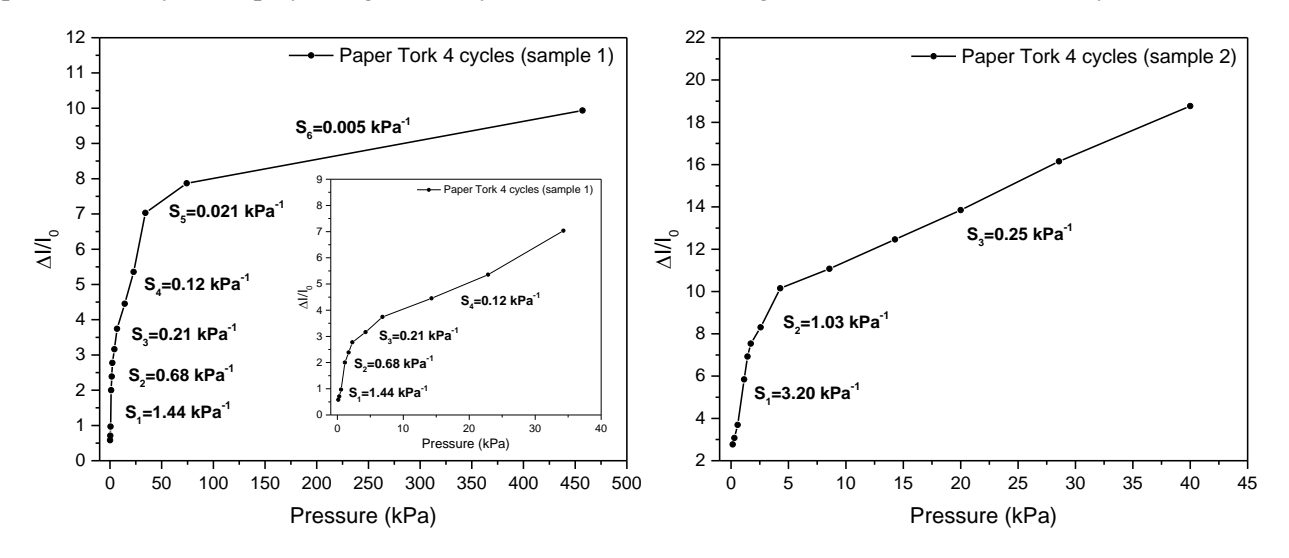


Figure 3.27 – Sensitivity test done on two sensors with 4 dip coating cycles paper Tork, with the potentiometer at 577Ω .

In Figure 3.27, the sensitivity test was done on two sensors with 4 dip coating cycles paper Tork and the potentiometer at 577 Ω . The 4 cycles paper had the highest resistance, while still forming a conductive AgNWs network. All the recorded pressures which were applied by a compression machine (so the pressure values were known) and their respective currents during the tests are in Table 3.4. For the first sensor (sample 1), the pressure was applied, its current value recorded and the sensor was return to its original state with only the initial current present, produced by the encapsulation pressure and the glass weight (distributes the pressure evenly), which is considered to be 0 kPa. The process was repeated for each applied pressure. For the second sensor (sample 2) a different initial current and a wait time of 15 s between applied pressures were used, to observe how the sensitivity would be affected. In both situations the sensor displayed good sensitivity values, however, these tended to decreased as the pressure increased. This was due to the low number of AgNWs at high pressures, which produces a lower ΔI for the same pressure increase and the voltage limitation caused by the potentiometer having a different resistance from the sensor, leading to an unbalanced voltage distribution.

Table 3.4 – Comparison between the currents and their respective pressures of the 2 sensors with 4 dip coating cycles paper Tork, with two different initial currents and the potentiometer at 577 Ω , displayed in Figure 3.27.

| | Paper Tork (0.7×0.5 cm) 4 cycles with the potentiometer at 577 Ω | | | | | | | | | | | | | | |
|------------|-------------------------------------------------------------------------|------|------|------|------|------|------|------|------|------|------|------|------|------|------|
| Sensor | Current (mA) | 0.21 | 0.34 | 0.37 | 0.42 | 0.64 | 0.72 | 0.81 | 0.89 | 1.02 | 1.17 | 1.36 | 1.73 | 1.91 | 2.35 |
| (sample 1) | Pressure (kPa) | 0 | 0.14 | 0.28 | 0.57 | 1.14 | 1.71 | 2.28 | 4.28 | 6.86 | 14.3 | 22.8 | 34.3 | 74.3 | 457 |
| Sensor | Current (mA) | 0.09 | 0.34 | 0.37 | 0.42 | 0.62 | 0.71 | 0.77 | 0.84 | 1.00 | 1.09 | 1.21 | 1.34 | 1.54 | 1.78 |
| (sample 2) | Pressure (kPa) | 0 | 0.14 | 0.28 | 0.57 | 1.14 | 1.43 | 1.71 | 2.57 | 4.28 | 8.57 | 14.3 | 20 | 28.6 | 40 |

The sensitivities for the different pressure ranges of sample 1 are 1.44 kPa⁻¹ (0.14-1.14 kPa), 0.68 kPa⁻¹ (1.14-2.28 kPa), 0.21 kPa⁻¹ (2.28-6.86 kPa), 0.12 kPa⁻¹ (6.86-34.28 kPa), 0.021 kPa⁻¹ (34.28-74.28 kPa) and 0.005 kPa⁻¹ (74.28-457 kPa). The current displayed a linear behaviour as the pressure increased in each range, except between 6.86-34.28 kPa. This was probably due to a disequilibrium in the pressure applied or the pressure hadn't stabilised, when the current value was recorded. In this sample the pressure limit was also tested and the sensor was able to reach a pressure of 457 kPa with a 2.35 mA of current. It's important to note

that although the 4 cycles paper sensor was able to reach that pressure, the sensitivity between 74.28-457 kPa was very low, so the optimal pressure limit was considered 74.3 kPa with 1.91 mA of current. The sample 2 sensitivity values are 3.20 kPa^{-1} (0.14-1.71 kPa), 1.03 kPa^{-1} (1.71-4.28 kPa) and 0.25 kPa^{-1} (4.28-40 kPa). This sample showed higher sensitivity values, due to its lower initial current of 0.09 mA and a more linear current behaviour, because of the 15 s wait time that enabled the compression machine to stabilise the applied pressure. The lowest and highest voltage detected on the oscilloscope of the 4 cycles paper Tork was 0.02V and 1.404V, which corresponds to $3.47 \times 10^{-5} \text{A}$ and $2.4 \times 10^{-3} \text{A}$, with an energy consumption of $6.94 \times 10^{-5} \text{W}$ and $4.8 \times 10^{-3} \text{W}$.

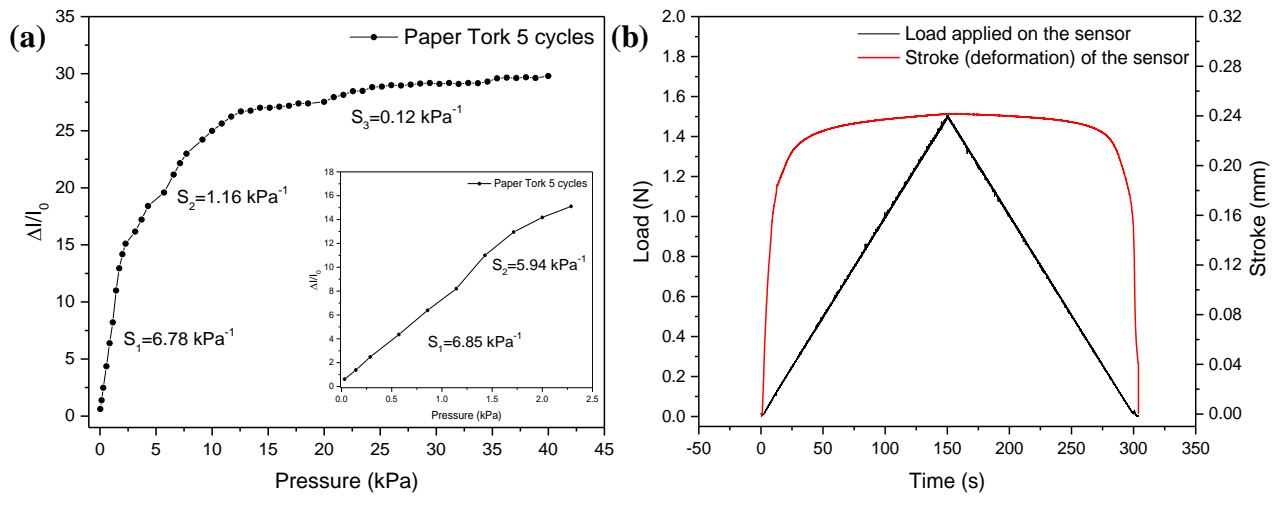


Figure 3.28 – (a) Sensitivity test done on the sensor with the 5 dip coating cycles paper Tork $(0.7\times0.5 \text{ cm})$ and the potentiometer at 577 Ω . (b) The compression/deformation of the sensor to the applied force during the test.

In Figure 3.28, the 5 cycles paper Tork sensor with the potentiometer at 577 Ω , was placed on the compression machine, with an initial current of 0.09 mA and a 0.01N/s of force applied. The sensitivity values are 6.78 kPa⁻¹ (0.031-2.28 kPa), 1.16 kPa⁻¹ (2.28-12.57 kPa) and 0.12 kPa⁻¹ (12.57-40 kPa). The maximum optimal pressure was 40 kPa with 2.77 mA, which is lower than the 4 cycles, however, the sensitivity values and the currents produced are higher, with the sensor being better at detecting small changes of pressure. The deformation of the sensor (mostly of the paper Tork) to the applied force was also recorded, in order to obtain an estimate of how much the sensor compresses with each force and its limit, which is around 0.242 mm.

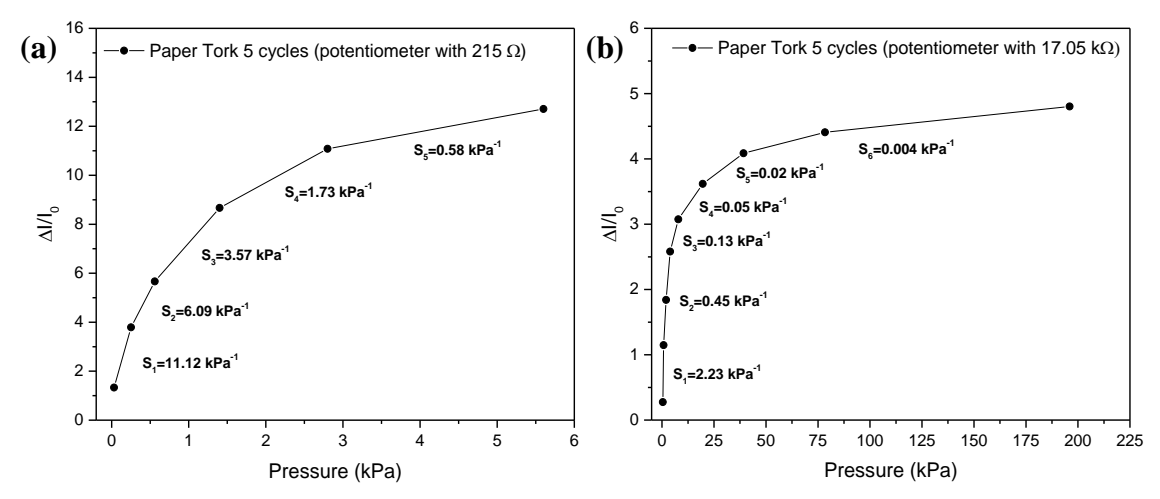


Figure 3.29 – Sensitivity tests done on the sensor. (a) On the 5 cycles paper Tork (0.7×0.5 cm), with the potentiometer at 215 Ω . (b) On the 5 cycles paper Tork (0.5×0.5 cm), with the potentiometer at 17.05 k Ω .

The sensor with the 5 dip coating cycles paper Tork was tested with different potentiometer resistances, to observe, how the current and sensitivity values would change, since at this time the resistance of the

AgNWs-tissue papers was unknown. The pressure on both samples was applied by weights (see Figure 6.9 in the Annexes). The results displayed in Figure 3.29-(a), were obtained while the potentiometer had a resistance of 215 Ω . The sensor displayed high sensitivity values at low pressures of 11.12 kPa⁻¹ (0.031-0.252 kPa), 6.09 kPa⁻¹ (0.252-0.56 kPa), 3.57 kPa⁻¹ (0.56-1.4 kPa), 1.73 kPa⁻¹ (1.4-2.8 kPa) and 0.58 kPa⁻¹ (2.8-5.6 kPa), which means that in order to detect lower pressures with a better sensitivity, a low potentiometer/sensor (since the potentiometer must match the sensor) resistance is desired. The lowest and highest voltage detected on the oscilloscope were 0.088 V and 1.416 V, which corresponds to 4.09×10^{-4} A and 6.59×10^{-3} A, with an energy consumption of 8.18×10^{-4} W and 1.32×10^{-2} W. The results of Figure 3.29-(b), showed the exact opposite, due to a high potentiometer resistance of 17.05 k Ω , the detectable initial current-voltage had a higher value than the first sample (215 Ω), which decreased the overall sensitivity values (the current-voltage-pressure values of both samples are displayed in Table 6.2 and Figure 6.10 in the Annex). However, the detectable pressure range was larger, with the highest recorded voltage being 2V, which is the value of the applied voltage on the sensor. So, in order to detect higher pressures, a high potentiometer/sensor resistance is desired. The lowest and highest voltage detected on the oscilloscope were 0.32 V and 2 V, which corresponds to 1.88×10^{-5} A and 1.17×10^{-4} A, with an energy consumption of 3.75×10^{-5} W and 2.34×10^{-4} W.

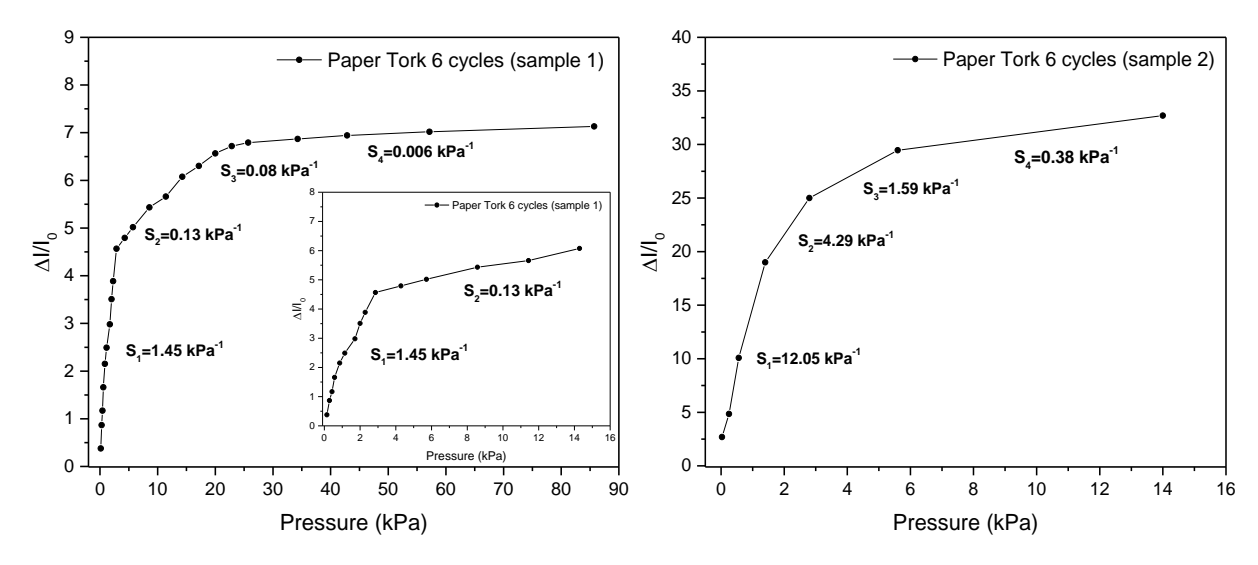


Figure 3.30 – Sensitivity test done on two sensors with 6 dip coating cycles paper Tork and the potentiometer at 577 Ω .

In Figure 3.30, the pressures applied on sample 1 were done by a compression machine (see Figure 6.10 in the Annexes) and on sample 2 by weights. The sensitivity values for sample 1 are 1.45 kPa⁻¹ (0.143-2.86 kPa), 0.13 kPa⁻¹ (2.86-14.3 kPa), 0.08 kPa⁻¹ (14.3-22.86 kPa) and 0.006 kPa⁻¹ (22.86-85.7 kPa). The initial current was 0.367 mA and the optimal pressure reached was 20 kPa with 2.78 mA of current. The values for sample 2 are 12.05 kPa⁻¹ (0.031-1.4 kPa), 4.29 kPa⁻¹ (1.4-2.8 kPa), 1.59 kPa⁻¹ (2.8-5.6 kPa) and 0.38 kPa⁻¹ (5.6-14 kPa). The initial current was 0.09 mA, which is lower than sample 1, increasing the sensitivity values significantly and the optimal pressure reached was 14 kPa with 3.04 mA. By analysing the results displayed on Table 6.3 in the Annexes, it can be observed that similar current values are present on both samples but with different pressures. This might be due to a decrease in the contact area between the weights and the sensor, which increased the applied pressure. However, the accurate current values for a given pressure are given by sample 1, since the force was applied by a compression machine. The lowest and highest voltage detected on the oscilloscope for the sensor with the 6 dip coating cycles paper Tork was 0.024 V and 1.748 V, which corresponds to 4.16×10⁻⁵ A and 3.03×10⁻³ A, with an energy consumption of 8.32×10⁻⁵ W and 6.06×10⁻³ W. Table 6.5 in the Annexes displays the sensitivity values of each sensor sample discussed in this section.

4

Conclusion and Future Perspectives

The original objective of this work to develop a low-cost paper-based flexible and wearable pressure sensor for health care by facile craft was achieved. All the components were produced successfully for a good sensor performance, considering that no previous work to build a paper-based sensor was done besides the AgNWs synthesis that had to be optimised. The AgNWs produced had 1-11 μ m of length and 45-80 nm of diameter, with a solution concentration of 0.75 mg/ml. The diffraction intensity ratio for the (111)/(200) planes was 5.48 and 19.61 for the (111)/(220) planes. The XRD analysis and the UV-Vis absorption spectrum of the OS solution showed that the AgNWs produced were in accordance with the ones observed in literature.

The BNC membranes created from the *nata de coco* cubes, had a high cellulose purity percentage and a crystalline index of 86%. Furthermore, the membranes displayed a UTS and fracture value of 126.36 MPa, with a very low deformation of 0.298 mm during the tensile test, which corresponds to an 23.85% increase in length of its original size and had a Young modulus of 693.46 MPa. The diameter values of both the fibers and pores were respectively, 44-59 nm and 35-68 nm. The membrane also presented a 78.41 nm RMS roughness (Sq) from a 100 μ m² scanning area and a 28.79 nm RMS roughness (Sq) from a 4 μ m² scanning area.

The IDEs printed on both the BNC and PET, had a resistance of 0.054 Ω /sq and 0.079 Ω /sq, respectively. After 500 folding cycles, the electrical resistance on the BNC increased from 0.5 Ω to 3.1 Ω , while on PET it increased from 1.1 Ω to 137 Ω . The IDEs on the BNC also had a 269.67 nm RMS roughness (Sq) from a 100 μ m² scanning area and a 35.63 nm RMS roughness (Sq) from a 4 μ m² scanning area.

Both spray and dip coating methods managed to coat the paper Tork successfully, with the OS exbiting a connected AgNWs network capable of conduction. The method implemented in the sensor construction was the dip coating method, however, better results could have been achieved by using a spray coating unit, turning the process autonomous. Paper Tork displayed the best results and was able to be implemented in the sensor, starting from 4 dip coating cycles, having a $26.08\pm7.33~\mathrm{k}\Omega$ at 6 cycles and up to $0.87\pm0.65~\mathrm{k}\Omega$ by 10 cycles.

For the sensor performance, the best response and recovery time, was achieved by using a paper Tork with 6 dip coating cycles, which presented a 0.8-1.6 ms response time and a 0.8 ms recovery time, for low fast pressures and 35.2 ms response time and a 16.8 ms recovery time for high prolonged pressures. In regards to the sensor stability, by observing small and large samples of currents, that were produced by equal and different applied pressures during the 15000 cycles of the stability test, it was possible to see that the sensor displayed

high stability throughout the test. However, after 15000 cycles, the sensor showed less stability than when it started, which is to be expected, but the values themselves did not changed significantly.

For the sensor sensitivity tests, papers Tork with 4, 5 and 6 dip coating cycles were used with various initial currents, two methods in which to apply the pressure (compression machine and weights) and different potentiometer resistances. The best achieved sensitivity values were 12.05 kPa⁻¹ (0.031-1.4 kPa), 4.29 kPa⁻¹ (1.4-2.8 kPa), 1.59 kPa⁻¹ (2.8-5.6 kPa) and 0.38 kPa⁻¹ (5.6-14 kPa) with the 6 cycles paper Tork and 0.25 kPa⁻¹ (4.28-40 kPa) with the 4 cycles paper Tork. A sensor/potentiometer with a low electrical resistance, is better in detecting low pressures, pressure changes and has better sensitivity values. A sensor/potentiometer with a high electrical resistance, has a larger detectable pressure range (can detect very high pressures), but at the cost of being worse in detecting low pressures and establishing a low initial current, which will result in lower sensitivity values. So a trade-off must be made, between having a sensor with high sensivity and being able to detect low pressures, or, having a larger detectable pressure range. The lowest and highest energy consumption from all the sensitivity tests done on the sensor with the paper Tork were 3.75×10⁻⁵ W and 1.32×10⁻² W.

In conclusion all the proposed objectives were achieved successfully aside from the heart rate pressure test, which can be done once the sensor is properly encapsulated, since a 31 Pa range is enough to detect it. The production cost of the sensor, for the complete process, was estimated to be around $1.79-2.3 \in$ and for the production of only 1 sensor to be $0.37-0.91 \in$, which makes it a paper-based flexible and wearable pressure sensor with low cost and of facile craft, with the use of only one expensive equipment. The AgNWs synthesis needs to be further optimised in order to produce larger and more NWs per synthesis, with lesser impurities and other nanostructures in the solution. Other synthesis methods could also be considered, especially a simple polyol synthesis, without the use of a microwave, which would turn the all process completely independent of any high cost equipment (when compared to the others used) and decrease the investment cost for the sensor fabrication, even further.

Testing how the automatic dip and spray coating process of the AgNWs on the tissue paper would effect its electrical resistance when compared to the manual process. Further experimentation with other types of paper. The type of BNC used, worked perfectly for the sensor, however, larger *nata de coco* samples would provide more margin for experimentation, with bigger IDEs being possible to print on its surface, which would result in a bigger sensor and henceforth the compression machine could applied smaller pressures in the <500 Pa range with more sensitivity and less variation. The BNC membrane could also be experimented in terms of its thickness and mechanical properties, for this, the freeze drying method should be tried and compared directly with the dry vacuum method. The pressure applied by both the manual and hydraulic press should also be adjusted, depending on the results of the drying methods used and in order to preserve the structural integrity of the membrane to folding, its surface smoothness and uniform thickness throughout the membrane.

The mechanical test to the glued membranes also managed to display a potential problem of the sensor when implemented on the skin, which is the absorption of sweat by the membrane, resulting in its expansion. This however, can be minimised by coating the membrane with a hydrophobic substance, like a vegetable oil or wax. The sensor can also be attached to the skin with enough pressure to limit its expansion during absorption, without significantly raising its initial current value. A hydrophobic glue with a good compatibility with the BNC membrane must also be found, to help in the sensor encapsulation. In regards to the sensor performance, more tests should be done, in order to determine the best possible paper electrical resistance for each specific detection range, to improve the sensor sensitivity. The use of a more elaborate and specific setup for the pressure sensor tests would help in the accuracy of the results obtained. The setup should be composed by a potentiostat, a compression machine with good sensitivity to low pressures and a computer. It should also be able to record all the necessary values for the characterization of the sensor at the same time.

5

References

- [1] Phanthong, P., Reubroycharoen, P., Hao, X., Xu, G., Abudula, A., & Guan, G. (2018). Nanocellulose: Extraction and application. Carbon Resources Conversion, 1(1), 32–43.
- [2] Bajpai, P. (2015). Green chemistry and sustainability in pulp and paper industry. Green Chemistry and Sustainability in Pulp and Paper Industry, 1–258.
- [3] Singh, A. T., Lantigua, D., Meka, A., Taing, S., Pandher, M., & Camci-Unal, G. (2018). Paper-based sensors: Emerging themes and applications. Sensors, 18(9), 1–22.
- [4] Prebianto, N. F., & Futra, A. D. (2018). Paper as a Substrate for Sensor Applications: A Review. Proceedings of the 2018 International Conference on Applied Engineering, ICAE 2018, 1–5.
- [5] Nery, E. W., & Kubota, L. T. (2013). Sensing approaches on paper-based devices: A review. Analytical and Bioanalytical Chemistry, 405(24), 7573–7595.
- [6] Islam, M. T., Alam, M. M., Patrucco, A., Montarsolo, A., & Zoccola, M. (2014). Preparation of nanocellulose: A review. AATCC Journal of Research, 1(5), 17–23.
- [7] Golmohammadi, H., Morales-Narváez, E., Naghdi, T., & Merkoçi, A. (2017). Nanocellulose in Sensing and Biosensing. Chemistry of Materials, 29(13), 5426–5446.
- [8] Mishra, R. K., Sabu, A., & Tiwari, S. K. (2018). Materials chemistry and the futurist eco-friendly applications of nanocellulose: Status and prospect. Journal of Saudi Chemical Society, 22(8), 949–978.
- [9] Salimi, S., Sotudeh-Gharebagh, R., Zarghami, R., Chan, S. Y., & Yuen, K. H. (2019). Production of Nanocellulose and Its Applications in Drug Delivery: A Critical Review. ACS Sustainable Chemistry and Engineering, 7(19), 15800–15827. review-article.
- [10] Kargarzadeh, H., Ioelovich, M., Ahmad, I., Thomas, S., & Dufresne, A. (2017). Methods for Extraction of Nanocellulose from Various Sources. Handbook of Nanocellulose and Cellulose Nanocomposites, 1–49
- [11] Rojas, J.; Bedoya, M.; Ciro, Y. Current Trends in the Production of Cellulose Nanoparticles and Nanocomposites for Biomedical Applications. Cellulose-Fundam. Aspects Curr. Trends 2015.
- [12] Alberto, E. L., de Ocampo, A. N., Depasupil, C. G., Ligaray, M., Eusebio, R. C., Orbecido, A., Patacsil, L. (2019). Acetylation of Nata de coco (bacterial cellulose) and membrane formation. MATEC Web of Conferences, 268, 04003.
- [13] Esa, F., Tasirin, S. M., & Rahman, N. A. (2014). Overview of Bacterial Cellulose Production and Application. Agriculture and Agricultural Science Procedia, 2, 113–119.
- [14] Rahmayanti, H. D., Amalia, N., Munir, R., Yuliza, E., Utami, F. D., Sustini, E., & Abdullah, M. (2019). A Study of Physical and Mechanical Properties of Nata de Coco in the Market. IOP Conference Series: Materials Science and Engineering, 599(1).
- [15] Langley, D., Giusti, G., Mayousse, C., Celle, C., Bellet, D., & Simonato, J. P. (2013). Flexible transparent conductive materials based on silver nanowire networks: A review. Nanotechnology, 24(45).
- [16] Lian, Y., Yu, H., Wang, M., Yang, X., & Zhang, H. (2020). Ultrasensitive wearable pressure sensors based on Silver nanowire-coated fabrics, 0–7.

- [17] Entifar, S. A. N., Han, J. W., Lee, D. J., Ramadhan, Z. R., Hong, J., Kang, M. H., Kim, Y. H. (2019). Simultaneously enhanced optical, electrical, and mechanical properties of highly stretchable transparent silver nanowire electrodes using organic surface modifier. Science and Technology of Advanced Materials, 20(1), 116–123.
- [18] Sohn, H., Park, C., Oh, J.-M., Kang, S. W., & Kim, M.-J. (2019). Silver Nanowire Networks: Mechano-Electric Properties and Applications. Materials, 12(16), 2526.
- [19] Kwon, J., Suh, Y. D., Lee, J., Lee, P., Han, S., Hong, S., ... Ko, S. H. (2018). Recent progress in silver nanowire based flexible/wearable optoelectronics. Journal of Materials Chemistry C, 6(28), 7445–7461.
- [20] Zhu, Y., Qin, Q., Xu, F., Fan, F., Ding, Y., Zhang, T., Wang, Z. L. (2012). Size effects on elasticity, yielding, and fracture of silver nanowires: In situ experiments. Physical Review B Condensed Matter and Materials Physics, 85(4), 1–7.
- [21] Elechiguerra, J. L., Larios-Lopez, L., Liu, C., Garcia-Gutierrez, D., Camacho-Bragado, A., & Yacaman, M. J. (2005). Corrosion at the nanoscale: The case of silver nanowires and nanoparticles. Chemistry of Materials, 17(24), 6042–6052.
- [22] Coskun, S., Aksoy, B., & Unalan, H. E. (2011). Polyol synthesis of silver nanowires: An extensive parametric study. Crystal Growth and Design, 11(11), 4963–4969.
- [23] Jang, H. W., Hwang, B. Y., Lee, K. W., Kim, Y. M., & Kim, J. Y. (2018). Controlling the size of silver nanowires produced by a tetrabutylammonium dichlorobromide salt-based polyol process: Kinetics of silver crystal growth. AIP Advances, 8(2).
- [24] Antonio de la Hoz, Angel Díaz-Ortiz and Pilar Prieto, CHAPTER 1: Microwave-Assisted Green Organic Synthesis, in Alternative Energy Sources for Green Chemistry, 2016, pp. 1-33.
- [25] Meléndrez, M. F., Medina, C., Solis-Pomar, F., Flores, P., Paulraj, M., & Pérez-Tijerina, E. (2015). Quality and high yield synthesis of Ag nanowires by microwave-assisted hydrothermal method. Nanoscale Research Letters, 10(1), 1–9.
- [26] Yi, Z., Xu, X., Tan, X., Liu, L., Zhang, W., Yi, Y., ... Tang, Y. (2017). Microwave-assisted polyol method rapid synthesis of high quality and yield Ag nanowires. Surface and Coatings Technology, 327(November 2018), 118–125.
- [27] Bannikoppa, S., Katageri, A. C., Balavalad, K. B., & Sheeparamatti, B. G. (2016). Design of Piezoresistive pressure sensor for enhanced sensitivity. 2016 International Conference on Energy Efficient Technologies for Sustainability, ICEETS 2016, (April), 706–710.
- [28] Gong, S., Schwalb, W., Wang, Y., Chen, Y., Tang, Y., Si, J., ... Cheng, W. (2014). A wearable and highly sensitive pressure sensor with ultrathin gold nanowires. Nature Communications, 5, 1–8.
- [29] Gao, L., Zhu, C., Li, L., Zhang, C., Liu, J., Yu, H.-D., & Huang, W. (2019). All Paper-Based Flexible and Wearable Piezoresistive Pressure Sensor. ACS Applied Materials & Interfaces, 11(28), 25034–25042. research-article.
- [30] Joo, Y., Byun, J., Seong, N., Ha, J., Kim, H., Kim, S., Hong, Y. (2015). Silver nanowire-embedded PDMS with a multiscale structure for a highly sensitive and robust flexible pressure sensor. Nanoscale, 7(14), 6208–6215.
- [31] Zhan, Z., Lin, R., Tran, V. T., An, J., Wei, Y., Du, H., ... Lu, W. (2017). Paper-Carbon Nanotube-Based Wearable Pressure Sensor for Physiological Signal Acquisition and Soft Robotic Skin. ACS Applied Materials and Interfaces, 9(43), 37921–37928.
- [32] Zhao, T., Li, T., Chen, L., Yuan, L., Li, X., & Zhang, J. (2019). Highly Sensitive Flexible Piezoresistive Pressure Sensor Developed Using Biomimetically Textured Porous Materials. ACS Applied Materials and Interfaces, 11(32), 29466–29473.
- [33] Wei, Y., Chen, S., Lin, Y., Yuan, X., & Liu, L. (2016). Silver nanowires coated on cotton for flexible pressure sensors. Journal of Materials Chemistry C, 4(5), 935–943.
- [34] Yang, C., Li, L., Zhao, J., Wang, J., Xie, J., Cao, Y., ... Lu, C. (2018). Highly Sensitive Wearable Pressure Sensors Based on Three-Scale Nested Wrinkling Microstructures of Polypyrrole Films. ACS Applied Materials and Interfaces, 10(30), 25811–25818.
- [35] Yang, J. C., Kim, J., Oh, J., Kwon, S. Y., Sim, J. Y., Kim, D. W., ... Park, S. (2019). Microstructured Porous Pyramid-Based Ultrahigh Sensitive Pressure Sensor Insensitive to Strain and Temperature. ACS Applied Materials & Interfaces, 11, 19472–19480.
- [36] Huang, Z., Gao, M., Yan, Z., Pan, T., Khan, S. A., Zhang, Y., Lin, Y. (2017). Pyramid microstructure with single walled carbon nanotubes for flexible and transparent micro-pressure sensor with ultra-high sensitivity. Sensors and Actuators, A: Physical, 266, 345–351.

- [37] Li, Y., Guo, S., Yang, H., Chao, Y., Jiang, S., & Wang, C. (2018). One-step synthesis of ultra-long silver nanowires of over 100 μm and their application in flexible transparent conductive films. RSC Advances, 8(15), 8057–8063.
- [38] Cao, L., Huang, Q., Cui, J., Lin, H., Li, W., Lin, Z., & Zhang, P. (2020). Rapid and facile synthesis of high-performance silver nanowires by a halide-mediated, modified polyol method for transparent conductive films. Nanomaterials, 10(6).
- [39] Ma, J., & Zhan, M. (2014). Rapid production of silver nanowires based on high concentration of AgNO3 precursor and use of FeCl3 as reaction promoter, 21060–21071.
- [40] Pa'E, N., Hamid, N. I. A., Khairuddin, N., Zahan, K. A., Seng, K. F., Siddique, B. M., & Muhamad, I. I. (2014). Effect of different drying methods on the morphology, crystallini-ty, swelling ability and tensile properties of nata de coco. Sains Malaysiana, 43(5), 767–773.
- [41] Tsouko, E., Kourmentza, C., Ladakis, D., Kopsahelis, N., Mandala, I., Papanikolaou, S., Koutinas, A. (2015). Bacterial cellulose production from industrial waste and by-product streams. International Journal of Molecular Sciences, 16(7), 14832–14849.
- [42] Tomer, G., Patel, H., Podczeck, F., & Newton, J. M. (2001). Measuring the water retention capacities (MRC) of different microcrystalline cellulose grades. European Journal of Pharmaceutical Sciences, 12(3), 321–325.
- [43] Campano, C., Balea, A., Blanco, A., & Negro, C. (2016). Enhancement of the fermenta-tion process and properties of bacterial cellulose: a review. Cellulose, 23(1), 57–91.
- [44] Gallegos, A. M. A., Carrera, S. H., Parra, R., Keshavarz, T., & Iqbal, H. M. N. (2016). Bacterial cellulose: A sustainable source to develop value-added products A review. Bi-oResources, 11(2), 5641–5655.
- [45] Klemm, D., Cranston, E. D., Fischer, D., Gama, M., Kedzior, S. A., Kralisch, D., ... Rauchfuß, F. (2018). Nanocellulose as a natural source for groundbreaking applications in materials science: Today's state. Materials Today, 21(7), 720–748.
- [46] Ferreira, N., Marques, A., Hugo, A., Bandarenka, H., Martins, R., Bodo, C., Silva, B., Fortunato, E. (2019). Label-Free Nanosensing Platform for Breast Cancer Exosome Profiling.
- [47] D. K. Schroder, Semiconductor Material and Device Characterization, 3rd Ed., Wiley (2016).
- [48] Kotatha, Di., & Rungrodnimitchai, S. (2018). Synthesis and Characterization of Nanofiber of Oxidized Cellulose from Nata de Coco. International Journal of Chemical Engineer-ing, 2018.
- [49] Segal, L., Creely, J. J., Martin, A. E., & Conrad, C. M. (1959). An Empirical Method for Estimating the Degree of Crystallinity of Native Cellulose Using the X-Ray Diffractome-ter. Textile Research Journal, 29(10), 786–794.
- [50] Rambo, M. K. D., & Ferreira, M. M. C. (2015). Determination of cellulose crystallinity of banana residues using near infrared spectroscopy and multivariate analysis. Journal of the Brazilian Chemical Society, 26(7), 1491–1499.
- [51] Chen, G., Wu, G., Chen, L., Wang, W., Hong, F. F., & Jönsson, L. J. (2019). Comparison of productivity and quality of bacterial nanocellulose synthesized using culture media based on seven sugars from biomass. Microbial Biotechnology, 12(4), 677–687.
- [52] Sardjono, S. A., Suryanto, H., Aminnudin, & Muhajir, M. (2019). Crystallinity and mor-phology of the bacterial nanocellulose membrane extracted from pineapple peel waste us-ing high-pressure homogenizer. AIP Conference Proceedings, 2120.
- [53] Halib, Nadia & Mohd Amin, Mohd Cairul Iqbal & Ahmad, Ishak. (2012). Physicochemical Properties and Characterization of Nata de Coco from Local Food Industries as a Source of Cellulose. Sains Malaysiana. 41. 205-211.
- [54] Kasim, A., Rahmi, I. D., Derosya, V., April, M., & April, M. (2017). Research Journal of Pharmaceutical, Biological and Chemical Sciences Characteristics of Nata de coco of Three Types Coconut Fermentation Media., 8(658), 658–664.
- [55] Reddy, N., & Yang, Y. (2015). Innovative Biofibers from Renewable Resources, 307–329.
- [56] Ashrafi, Z., Lucia, L., & Krause, W. (2019). Bioengineering tunable porosity in bacterial nanocellulose matrices. Soft Matter, 15(45), 9359–9367.

6

Annexes

Disregarding the only conductive SS solution that managed to properly coat the paper. Spray coating alone could not make the paper conduct with the SS solution and could take up to 1 hour, which is time consuming and unnecessary, even with high concentrated solutions it would still not conduct. This is due to various reasons, one of them is human error during spray deposition in which some areas would be more covered in AgNWs, while leaving empty space on others. The other reason would be the high number of small AgNWs present in the SS solution, which increases the probability of the wires not connecting with each other. There is also the possibility that some of them are still coated with PVP, which would affect their conductivity.



Figure 6.1 – Spray coating process on a glass substrate and measuring of its electrical resistance with a multimeter.

To know if the SS solution would be able to make a non-porous substrate conduct, a glass substrate was used. The coffee ring effect was worse on glass than on the paper, which resulted in most AgNWs to deposit away from the center. After measuring its resistance with a multimeter, it was confirmed that the problem was with the paper substrate, more specifically with its porosity, since a non-porous material like glass could be made conductive by using the same solution. So, in order to compensate for the porosity of the paper and to make the paper conduct, while also decreasing the amount of solution used, laser welding was applied to the paper to weld the junction sections between the AgNWs to improve conductivity. To do this process, a 4 cm² tissue paper was spray coated with 3 ml of the SS solution and a matrix was created to test different powers and velocities during laser welding. After various tests the laser beam with 5 Watts and 0.762 m/s, and 6.5 Watts with 1.016 m/s produced the best results, without damaging the paper fibers too much. However, the paper structural integrity was still compromised and couldn't be used for the sensor.

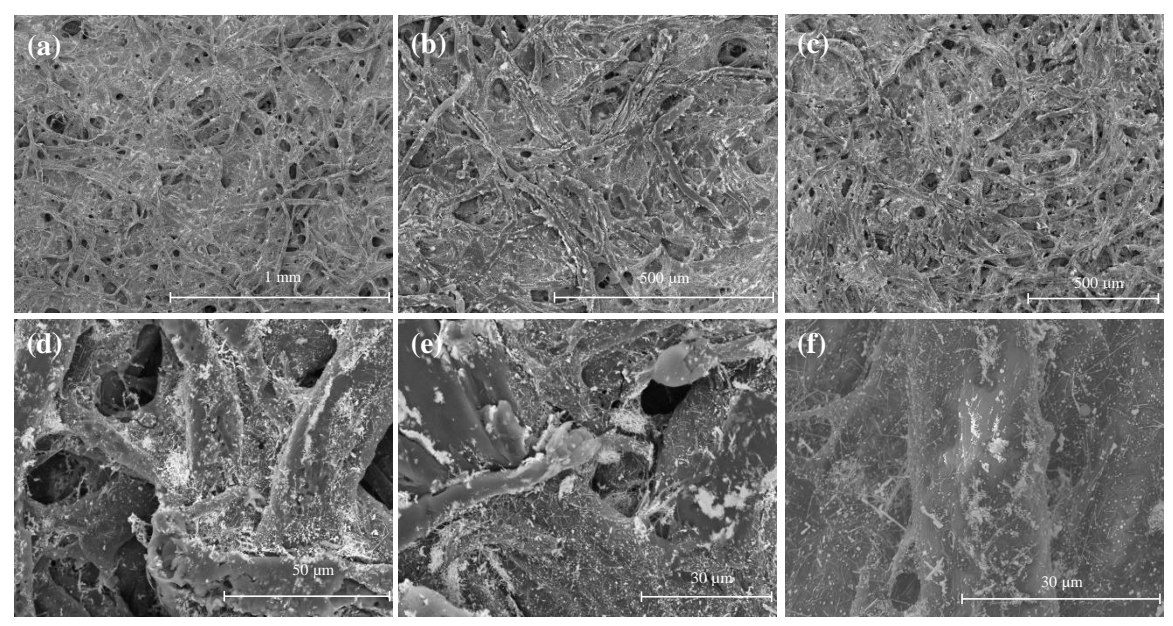


Figure 6.2 – Laser welding of the paper Whatman coated with 3 ml of the AgNWs solution produced with the SS. (a,d) paper Whatman without welding; (b,e) welding with 5 watts and 0.762 m/s; (c,f) welding with 6.5 watts and 1.016 m/s.

The conductivity achieved on the paper Whatman with laser welding reached as low as $16 \Omega/\text{sq}$, but at the cost of burning the fibres compromising its structural integrity. This would be a good result if the objective was to create a conductive paper, however for the sensor to work properly, the mechanical properties and structure of the fibers needs to remain as unchanged as possible from their original state, in order to improve the sensor performance. So, in the end this option was discarded.

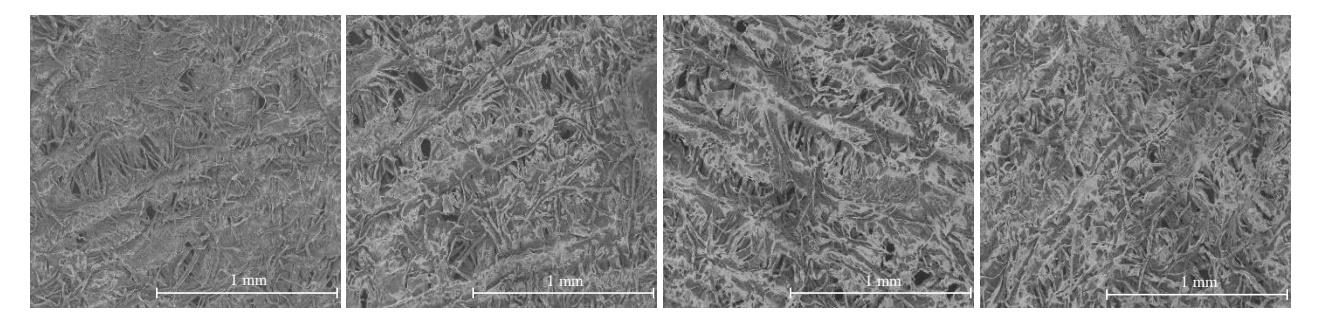


Figure 6.3 - SEM images of the paper Tork coated with AgNWs from an OS solution, each image shows the increase in the NWs coverage with each dip coating cycle. The images correspond respectively to 4,6,8,10 cycles (left to right).

The images above correspond respectively to the 4,6,8,10 dip coating cycles on the paper Tork and show a better perspective of how much the number of AgNWs increases throughout the paper with each cycle. Until the 4 cycles mark is reach, there is little contrast change that can be detected. The most significant difference happens between the 4 and 6 cycles where the amount of AgNWs increases exponentially, which is probably due to the anchorage effect (the new NWs coated with each cycle will anchor to the existing ones already on the paper). The amount of AgNWs continues to increase with each cycle and by 10 dip coating cycles, it achieves full coverage, however, due to the filter used, the differences are barely noticeable, so it may appear that the paper does not have full NW coverage. In order to have a better view the AgNWs coverage, the SEM images of the dip coated Kimberly paper can be seen on Figure 6.4 bellow. This paper has a higher porosity than the Tork paper, it is also thinner, has less fiber density and still managed to achieve full coverage.

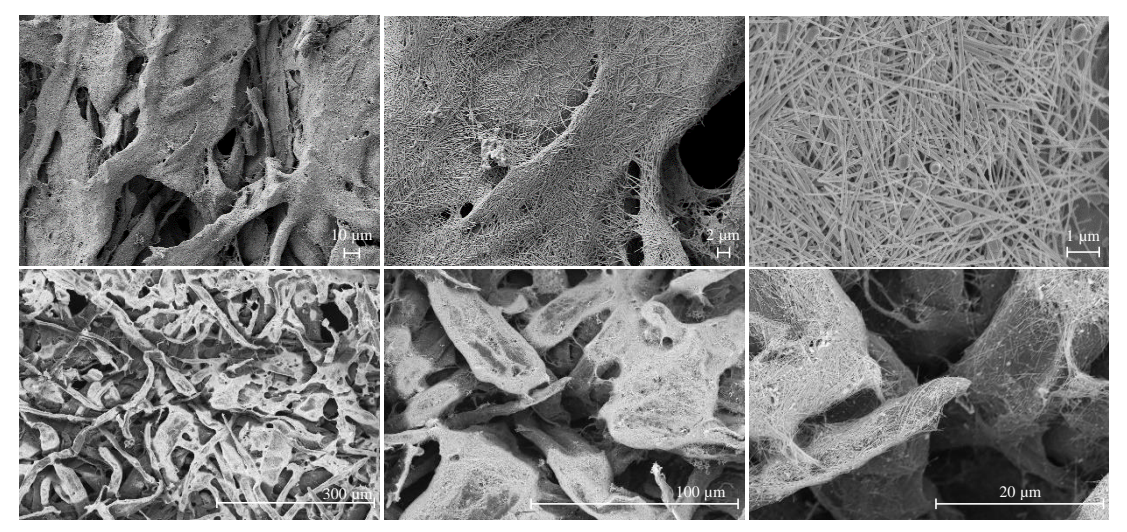


Figure 6.4 – SEM images with the SEM-FIB (no filter) and Hitachi Tabletop SEM (filter that highlights the contrast areas with high and low AgNWs density) of the Kimberly paper with 10 dip coating cycles, fully covered with AgNWs of the OS, exhibiting a resistance of $6.35\pm3.04~\mathrm{k}\Omega/\mathrm{sq}$.

Table 6.1 – Quantities and prices of the products, bought in bulk, used during the fabrication of the necessary components to produce the sensor and to fabricate one sensor.

| | Products used to fabricate the pressure sensor and their prices | | | | | | | | | | | |
|-------------------------|-----------------------------------------------------------------|----------------------|---------------------------------|-------------------|------------------|-----------------|----------------|----------------------|----------------------|------------|--|--|
| Products | AgNO ₃ | EG | NaCl | PVP | Acetone | IPA | Methanol | BNC | Silver Ink | Total | | |
| Product Bought | 343.44 € 0.1 Kg | 17,91 € 1 L | 21,90 € 1 Kg | 38.10 € 0.1 Kg | 17,92 € 5 L | 21,65 € 5 L | 26.80 € 1 L | 200–300 € 1 Ton | 184.00 € 2 L | 872-972 € | | |
| Product Used | 0.31 € 0.09 g | 0.31 € 17.5 ml | 1×10 ⁻⁴ € 0.005 g | 0.03 € 0.075 g | 0.32 € 100 ml | 0.13 € 30 ml | 0.4 € 15 ml | 0.2-0.4 € 2 cubes | 0.09-0.4 € 1-4 ml | 1.79-2.3 € | | |
| Product for 1 sensor | 10 ml of 1.5 € so s | 0.2-0.4 € 2 cubes | 0.09-0.4 € 1-4 ml | 0.37-0.91 € | | | | | | | | |

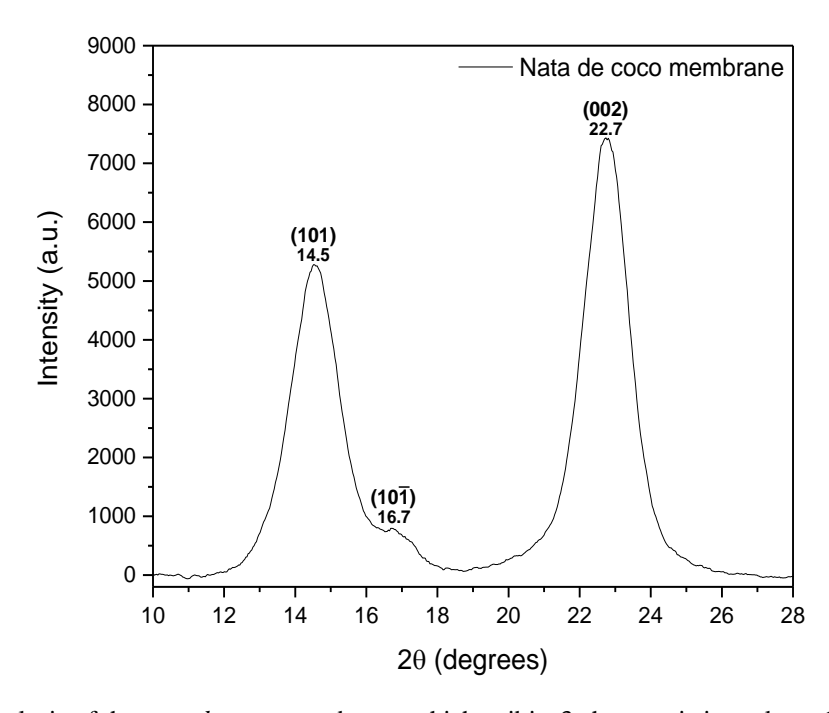


Figure 6.5 – XRD analysis of the nata de coco membrane, which exibits 3 characteristic peaks at 14.5°, 16.7° and 22.7°.

The *nata de coco* XRD spectrum has 3 peaks at 14.5° , 16.7° and 22.7° , which are consistent with the ones present in literature [46][48] and indicate the presence of both I α and I β crystal cellulose. These peaks correspond respectively to the crystalline planes (101), (10 $\overline{1}$) and (002) and although there are 3 distinguishable peaks, the peaks at 16.7° and 14.5° convolute with each other. This might mean the presence of amorphous substances, which were not removed during the cleaning process prior to use or were introduced to the nata de coco surface during the membrane fabrication. The crystalline index (**CrI**) was determined using Segal's equation [49], with a more detailed explanation of the process found at Rambo & Ferreira et al. (2015) [50]. The values were calculated without any baseline subtraction of the XRD spectrum, where ($\mathbf{I_{am}}$) is the minimal intensity value of the amorphous region around 18° and ($\mathbf{I_{002}}$) is the maximum intensity value of the peak at 22.7° from the crystalline region. This resulted in a crystalline index of 86%, with the BNC presenting a very high value when compared to other BC in literature [51][52].

$$CrI = \frac{I_{200} - I_{am}}{I_{200}} \times 100$$
 equation (6.1)

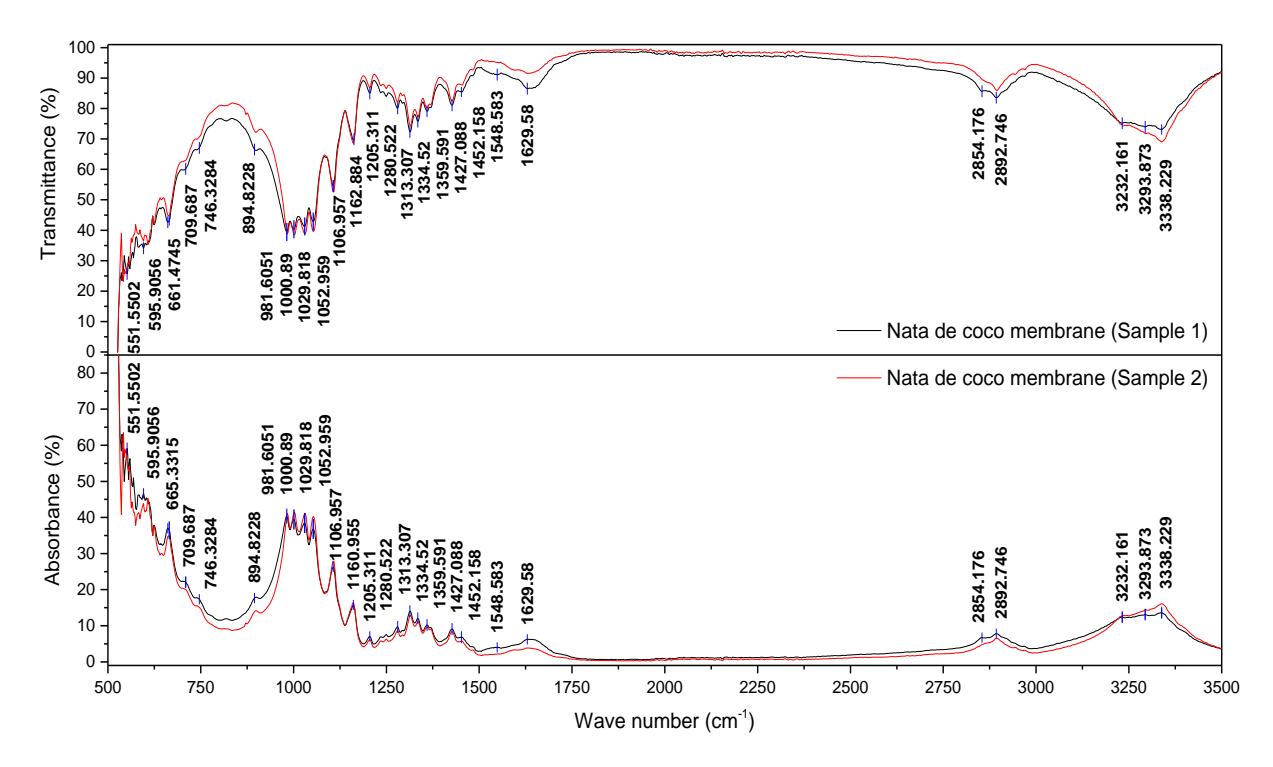


Figure 6.6 – FTIR analysis of the transmittance and absorbance spectre of two *nata de coco* membrane samples.

The BNC membrane was submitted to an FTIR analysis to verify its purity and the presence of other non-cellulose substances. The FTIR spectrum revealed 8 characteristic peaks of BC at 895 cm⁻¹, 1029 cm⁻¹, 1106 cm⁻¹, 1160 cm⁻¹, 1313 cm⁻¹, 1427 cm⁻¹, 2892 cm⁻¹ and 3348 cm⁻¹. According to literature [53] pure cellulose has distinguished peaks around 3350 cm⁻¹ indicating O-H stretching, 2800-2900 cm⁻¹ indicating C-H stretching, 1400 cm⁻¹ indicating CH₂ bending, 1300 cm⁻¹ indicating C-H bending and 1160 cm⁻¹ indicating C-O-C stretching. By comparing the peaks of the samples from this work with the ones from pure cellulose, it proves that the BNC membranes created from the nata de coco cubes have a high cellulose purity percentage. Furthermore, all the peaks in the FTIR spectrum of the samples analysed are present in other FTIR spectrums of *nata de coco* found in literature [46][54].

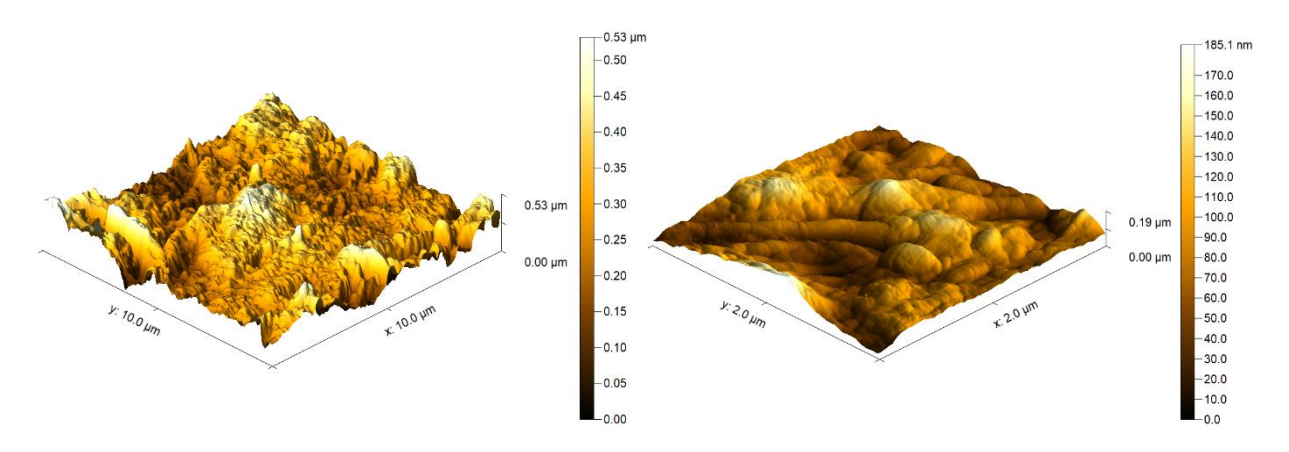


Figure 6.7 – AFM 3D morphological images of the membrane surface through the use of the Gwyddion software.

The 3D images above were generated with the Gwyddion software, by processing the data aquired through AFM analysis which enables a more detailed view of the membrane morphology and allows the determination of its rugosity. The images of the membrane displayed on Figure 6.7 have a 78.41 nm RMS roughness (Sq) from a 100 μ m² scanning area and a 28.79 nm RMS roughness (Sq) from a 4 μ m² scanning area. These values are within the range of results of other BC in literature [55][56].

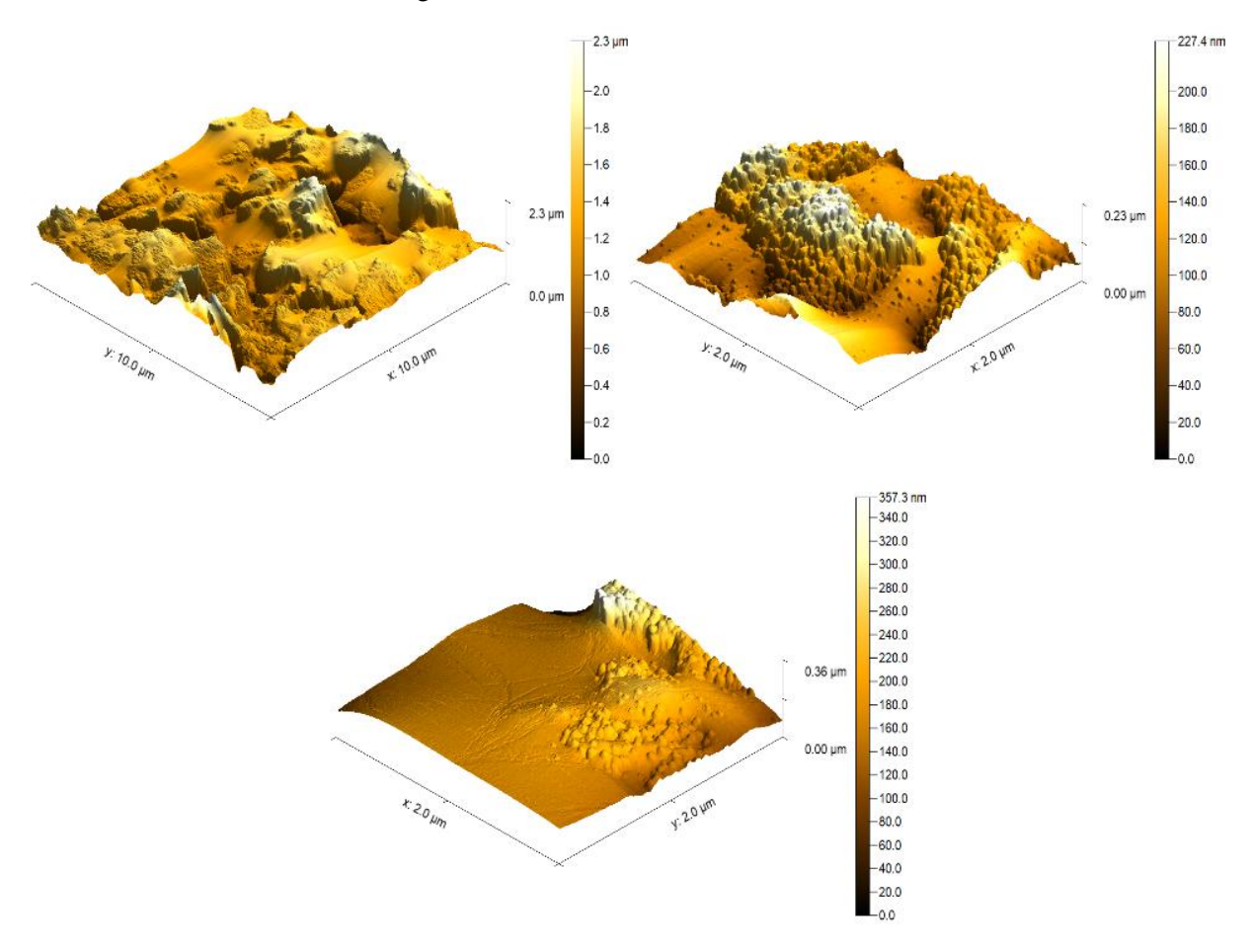


Figure 6.8 - AFM 3D morphological images of the finger electrodes surface through the use of the Gwyddion software.

Figure 6.8 above displays the AFM analysis results of the finger electrodes surface. Their surface has a 269.67 nm RMS roughness (Sq) value from a 100 μ m² scanning area and a, 37.70 nm and 35.63 nm RMS roughness (Sq) value from a 4 μ m² scanning area.



Figure 6.9 – Setup (sensor, probes and the KEYSIGHT 33500B series waveform generator) with the weights used during the sensitivity tests to apply specific pressures on the sensor.

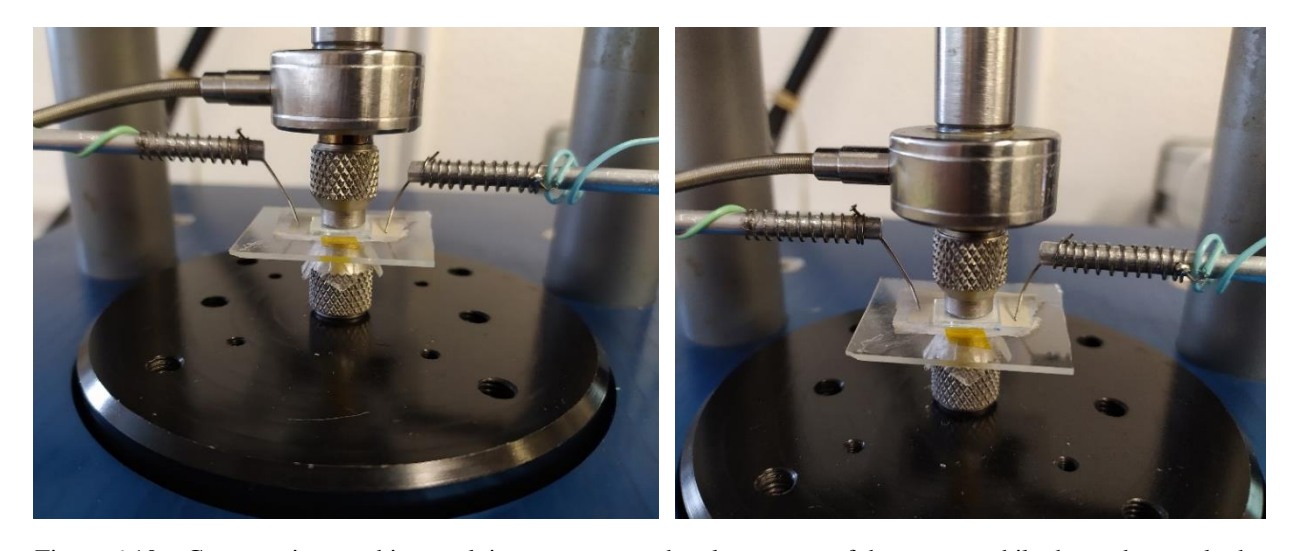


Figure 6.10 – Compression machine applying pressure on the glass on top of the sensor, while the probes apply the voltage supplied by the KEYSIGHT 33500B series waveform generator, to the interdigitated electrodes pads.

Table 6.2 - Comparison between the currents and their respective pressures of one 5 dip coating cycles paper Tork sample (0.7×0.5 cm), with the potentiometer at 215 Ω , to another 5 dip coating cycles paper Tork sample (0.5×0.5 cm), with the potentiometer at 17.05 k Ω . Their sensitivity plots are displayed in Figure 3.29

| | Paper Tork with 5 dip coating cycles with the potentiometer at 215 Ω and 17.05 k Ω | | | | | | | | | | | |
|-------------|--------------------------------------------------------------------------------------------------|-------|-------|-------|-------|-------|-------|-------|-------|-------|-------|--|
| Sample with | Current (mA) | 0.45 | 1.04 | 2.14 | 2.98 | 4.32 | 5.40 | 6.12 | / | / | / | |
| 215 Ω | Pressure (kPa) | 0 | 0.031 | 0.252 | 0.56 | 1.4 | 2.8 | 5.6 | / | / | / | |
| Sample with | Current (mA) | 0.019 | 0.024 | 0.040 | 0.054 | 0.068 | 0.077 | 0.088 | 0.097 | 0.103 | 0.110 | |
| 17.05 kΩ | Pressure (kPa) | 0 | 0.392 | 0.784 | 1.96 | 3.92 | 7.84 | 19.6 | 39.2 | 78.4 | 196 | |

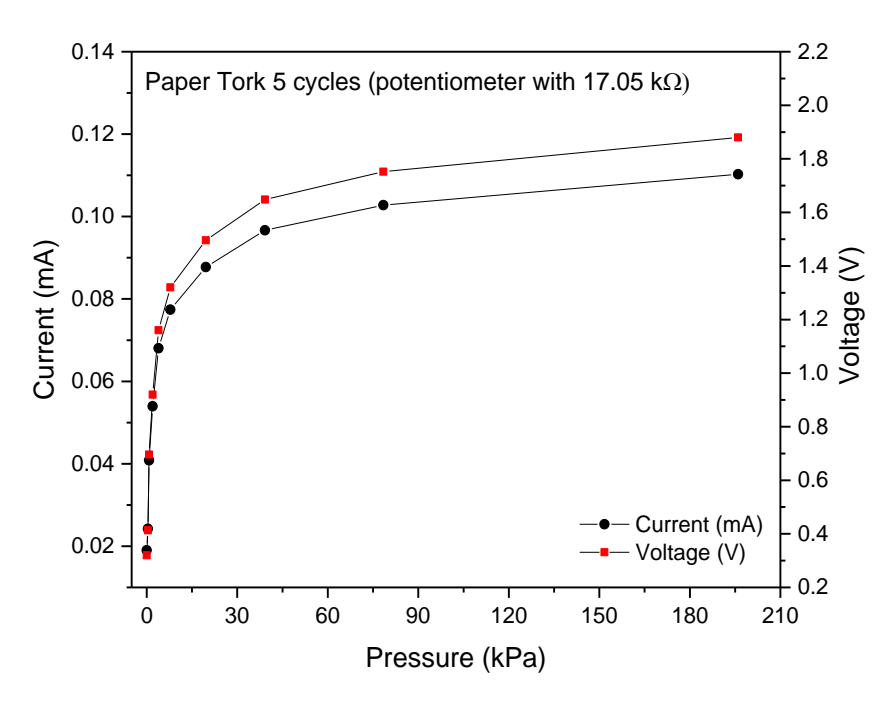


Figure 6.11 - Current-Voltage-Pressure plot of the 5 dip coating cycles paper Tork (0.5×0.5 cm) with the potentiometer at 17.05 $k\Omega$, with the respective sensitivity results displayed on Figure 3.29 and the exact values on Table 6.2.

Table 6.3 - Comparison between the currents and their respective pressures of the two sensors (sample 1 and sample 2) with 6 dip coating cycles paper Tork, with two different initial currents and the potentiometer at 577 Ω . Their sensitivity results are displayed in Figure 3.30

| | Paper Tork (0.7×0.5 cm) 6 cycles with the potentiometer at 577 Ω | | | | | | | | | | | | | | |
|----------|-------------------------------------------------------------------------|-------|-------|------|------|------|------|------|------|------|------|------|------|------|------|
| C | Current (mA) | 0.367 | 0.51 | 0.69 | 0.80 | 0.98 | 1.16 | 1.28 | 1.46 | 1.79 | 2.21 | 2.36 | 2.60 | 2.78 | 2.99 |
| Sample 1 | Pressure (kPa) | 0 | 0.14 | 0.28 | 0.43 | 0.57 | 0.86 | 1.14 | 1.71 | 2.28 | 5.71 | 8.57 | 14.3 | 20 | 85.7 |
| G 1. 2 | Current (mA) | 0.09 | 0.33 | 0.52 | 0.99 | 1.80 | 2.34 | 2.74 | 3.04 | / | / | / | / | / | / |
| Sample 2 | Pressure (kPa) | 0 | 0.031 | 0.25 | 0.56 | 1.4 | 2.8 | 5.6 | 14 | / | / | / | / | / | / |

Table 6.4 – Paper types used for the dip and spray coating method during the tissue paper coating process.

| | | Paper Types | |
|------|-----------------|-----------------|------------------|
| Tork | Kimberly-Clarke | Whatman Grade 2 | Paper from Korea |

Table 6.5 – Sensitivity values of each sensor sample tested in the sensitivity tests.

| | | Sensitivity | values of the s | ensor samples | S | |
|------------------------|----------------------------------------------|--------------------------------------------|--------------------------------------------|---------------------------------------------|----------------------------------------------|--------------------------------------------|
| 4 cycles (sample 1) | 1.44 kPa ⁻¹ (0.14-1.14 kPa) | 0.68 kPa ⁻¹ (1.14-2.28 kPa) | 0.21 kPa ⁻¹ (2.28-6.86 kPa) | 0.12 kPa- ¹ (6.86-34.28 kPa) | 0.021 kPa ⁻¹ (34.28-74.28 kPa) | 0.005 kPa ⁻¹ (74.28-457 kPa) |
| 4 cycles (sample 2) | 3.20 kPa ⁻¹ (0.14-1.71 kPa) | 1.03 kPa ⁻¹ (1.71-4.28 kPa) | 0.25 kPa ⁻¹ (4.28-40 kPa) | / | / | / |
| 5 cycles (577 Ω) | 6.78 kPa ⁻¹ (0.031-2.28 kPa) | 1.16 kPa ⁻¹ (2.28-12.57 kPa) | 0.12 kPa ⁻¹ (12.57-40 kPa) | / | / | / |
| 5 cycles (215 Ω) | 11.12 kPa ⁻¹ (0.031-0.252 kPa) | 6.09 kPa ⁻¹ (0.252-0.56 kPa) | 3.57 kPa ⁻¹ (0.56-1.4 kPa) | 1.73 kPa ⁻¹ (1.4-2.8 kPa) | 0.58 kPa ⁻¹ (2.8-5.6 kPa) | / |
| 5 cycles (17.05 kΩ) | 2.23 kPa ⁻¹ (0.392-0.784 kPa) | 0.45 kPa ⁻¹ (0.784-3.92 kPa) | 0.13 kPa ⁻¹ (3.92-7.84 kPa) | 0.05 kPa ⁻¹ (7.84-19.6 kPa) | 0.02 kPa ⁻¹ (19.6-39.2 kPa) | 0.004 kPa ⁻¹ (39.2-196 kPa) |
| 6 cycles (sample 1) | 1.45 kPa ⁻¹ (0.143-2.86 kPa) | 0.13 kPa ⁻¹ (2.86-14.3 kPa) | 0.08 kPa ⁻¹ (14.3-22.86 kPa) | 0.006 kPa ⁻¹ (22.86-85.7 kPa) | / | / |
| 6 cycles (sample 2) | 12.05 kPa ⁻¹ (0.031-1.4 kPa) | 4.29 kPa ⁻¹ (1.4-2.8 kPa) | 1.59 kPa ⁻¹ (2.8-5.6 kPa) | 0.38 kPa ⁻¹ (5.6- 14 kPa) | 1 | / |

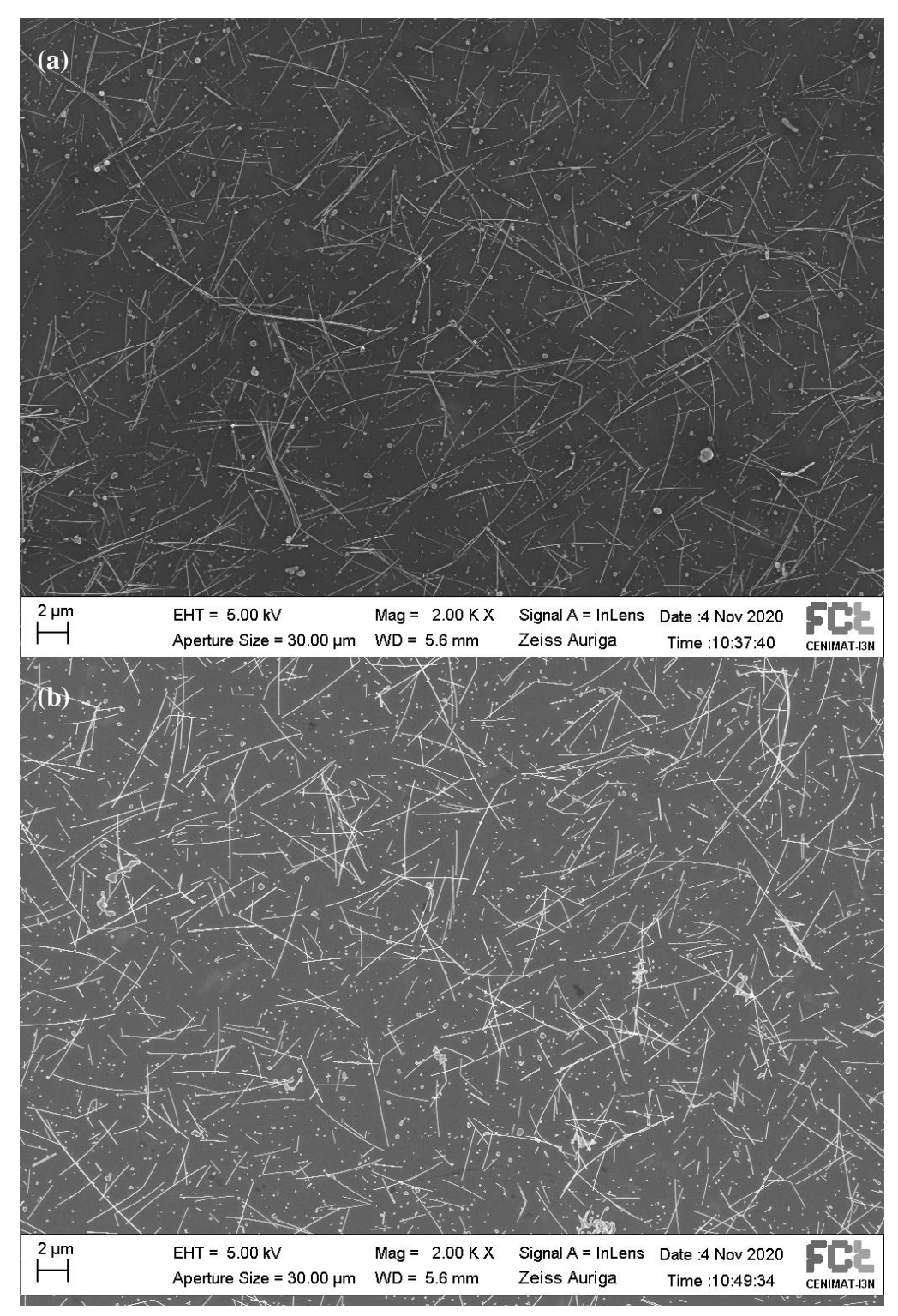


Figure 6.12 – High quality SEM images of the OS solution used to measure the AgNWs dimensions. (a) AgNWs after the first purification (acetone decantation); (b) AgNWs after the final purification (acetone and IPA decantation).

On Figure 6.12 – (a) 76 AgNWs were measured with the ImageJ software and they had a length between 1-11 μ m, with an average value of 6.42 \pm 2.20 μ m and on Figure 6.12 – (b) 80 AgNWs were measured and had a length between 1-11 μ m, with an average value of 6.38 \pm 1.54 μ m. The more purifications done on the solution the higher the risk of NW fractures, which will decrease their length.